Student
R.G. Nieboer (0490075)

Supervision

Prof. dr. Ruud Schotting
Utrecht University

Drs. Nick Buik
IF-technology

MSc Thesis, date
August 14, 2012

Thermal hydrological modeling of the effect of fault zones intersecting primary porous media and the implications for enhancing Geothermal exploration potential at shallower depths

Abstract

For geothermal energy exploration, depth to required fluid temperature and potential extraction rates are important factors for economical viability. Local thermal anomalies found in boreholes might be associated with convective flow through faults. This research applies a finite element modeling method to investigate the effect of high permeability faults on large-scale convection in a sedimentary basin, roughly resembling the North Sea basin. An extensive literature review is included in an attempt to impose realistic permeability properties on basins and fault zones. Though frequently faults are considered to be 'sealing', this is only in the fault normal direction resulting from grain reduction in the core of the fault. The fracture network located at both sides of the core can, under certain conditions, become very permeable in the along fault direction. It was found that when faults are closely spaced, thermal convection originates even when the enveloping basin has too low conductive properties to start convecting itself. Significant temperature anomalies are produced that might indeed be utilized for geothermal exploration, where the high fault permeability can act as an extraction rate enhancer.

Content

1. Introduction

The demand for energy is still rising and fossil fuels reserves shrink rapidly. The awareness of the human influence on the environment has put strong emphasis on renewable energy developments. A major player in this field is geothermal energy, because it is sustainable, environmentally friendly and has very large potential (Tester et al. 2006).

The development of deep geothermal heat mining expanded the exploitable area. From limited to plate boundaries, now it is possible nearly everywhere depending on the available funding for exploration and drilling. By drilling into a preferably highly porous and permeable reservoir, depths can be reached where fluids have temperatures that are sufficient for surface use in (district) heating or electricity production. A circulatory tract has to be established where cold fluid is pumped in and hot fluid is extracted after it is conductively heated by the naturally occurring hot rock. When the obtained flow rates aren't economically sufficient, the reservoir can be pressurized in order to create shear stress relief, which can increase the permeability. When using this hydraulic stimulation, often combined with chemical and thermal stimulation and by addition of proppants (Willemsen et al. 2011), this is called a Enhanced or Engineered Geothermal System (EGS).

Permeability is the key variable for rocks to be candidate as a geothermal reservoir. Therefore, rocks should inhibit primary porosity or fractures and must exhibit brittle behavior for stimulation. Strongly lithified highly porous sandstones and naturally fractured limestones, igneous and metamorphic rocks are good sources, evaporates and high clay content sediments are poor because upon hydraulic fracturing they deform by plastic deformation and 'smearing' respectively. Locating favorable facies can be performed by for instance seismic interpretation or core data.

Higher, more preferable, geothermal gradients can be found by measuring heat flow at depth combined with variable geophysical measurements. Magnetic surveys can be used to find the Curie point at depth. Ferromagnetic minerals lose their magnetic susceptibility at a critical (Curie) temperature. This temperature is different for different minerals and defines isotherm depths (e.g. Ates et al. 2005), which deviations from a reference temperature frame can be used to locate preferential sites heat mining. Magnetotellurics can be used to detect circulation of geothermal brines by measuring electrical conductivity anomalies. These measurements can be complemented by gravimetric methods. When the subsurface geology is known from seismic imaging and basin models, negative Boguer anomalies indicating a mass deficit can be associated with relative low density facies that have been subject to strong fracturing which may act as conduits for geothermal circulation (Schill et al. 2010).

Another potentially favorable condition, and object of this study, is the presence of fault systems in the above mentioned reservoir rocks. Fault zones are indicated as potential agents for thermal advective flow. Local, small wavelength (<10 km) thermal anomalies are attributed to faults by many studies (e.g. McKenna & Blackwell 2004; Fleming et al. 1998; Simms et al. 2004). A local example comes from borehole temperature measurements in the area of Amsterdam, the Netherlands. Here a deviation of +20 K with respect to the expected temperature field is found, in the proximity of a major fault zone (Willemsen et al. 2011). In contrast, features like intruding granite show more regional anomalous heat flows and gravity anomalies.

The goal of this research is to test the following hypothesis:

The presence of permeable fault zones in primary porous rock increase the geothermal potential of an EGS system as they can act as agents for buoyant thermal upwelling and higher extraction rates. Higher temperatures are found at shallower depths and can more easily be mined, making geothermal energy more lucrative and thus more competitive with environmentally unfriendly hydrocarbon exploration.

Though in principle this model study is of fundamental scientific nature, it roughly envelops the properties of the North-Sea basin with respect to (average) values for e.g. geothermal gradient, basin thickness and permeabilities.

The most important variables for testing this hypothesis are *fault zone architecture and permeability structure* and *thermal convection* that will be discussed in depth in the next 2 Sections.

2. Fault zone architecture and permeabilities

In situ fault zone permeability structures are very complex and therefore difficult to predict. The dimensions of the finer features fall below the resolution of seismic surveys. Though wells give some, mostly lithological information, the strong heterogeneity of a fault zones gives little room for extrapolation or for upscaling. Good interpretations can come from surface field data, when studies are performed in different geological settings (e.g. lithology, stress regime).

This study uses the major fault components; fault core, damage zone and protolith, defined by Chester & Logan (1987) as a research framework (Fig. 1). The fault core is a fine grained, poorly sorted, low permeable cataclasite or gouge over which the bulk of the fault's displacement has taken place. The damage zone lies adjacent to the fault core and is characterized by small faults and fractures originating from the stress field caused by the slip accommodated in the fault core. The undisturbed host rock is defined as protolith, where the permeability is not a product of fault displacement, but comes from primary porosity, if present. Not all of the above mentioned components have to be present in any fault zone, nor can they be considered as steady-state with respect to fluid flow properties (Caine et al. 1996)

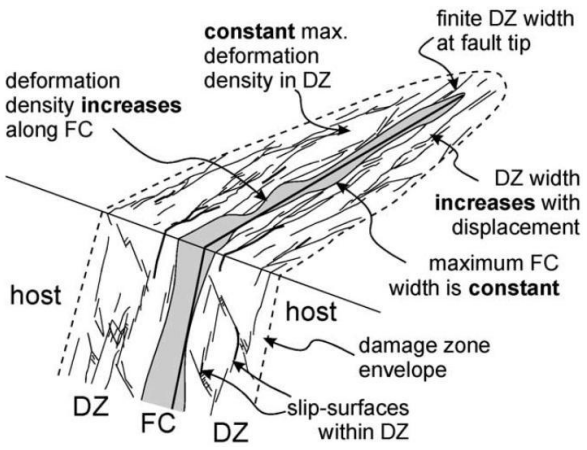

Fig. 1: Fault components: fault core and damage zone within undeformed host rock. Maximum deformation density in the damage zone, refers to the proposed transition to cataclistic deformation accompanied by strain hardening (Z.K. Shipton & Cowie 2003)

Conceptual permeability geometries

A range of permeability geometries are observed and interpreted from field data. In Fig. 2 four end-member architectural styles, based on the degree of development of damage zone and fault core are defined (Caine et al. 1996). When considering the North Sea basin, only sedimentary material, predominantly sandstones and shales are encountered. So only 'localized barrier' and 'conduit-barrier' schemes apply because a fault core in the form of deformation band or cataclistic gouge will inevitably form.

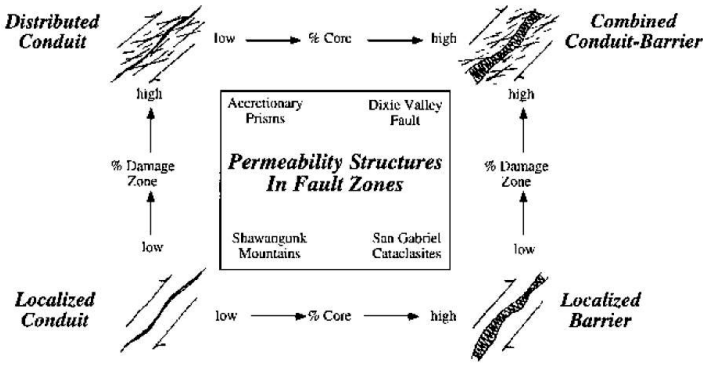

Fig. 2: End-member architectural styles for fault zones. For cataclistic fault deformation, as are found in sandstones, there's always a well developed fault core present. (Caine et al. 1996)

The localized barrier is a classic fault seal that can be recognized by discontinuities in hydraulic head on either side of a fault that compartmentalizes regional flow systems (e.g. Bredehoeft et al. 1992). In this scheme, lateral (fault normal direction) as well as

longitudinal (fault parallel direction) fault permeabilities impede fluid flow. This is the key difference with the conduit-barrier scheme. Short wavelength geothermal anomalies (e.g. McKenna & Blackwell 2004) and mineralization patterns (Mozley & Goodwin 1995) show that faults can have high hydraulic conductivity in the fault parallel direction even if the normal direction is sealed. For these cases it is clear that the permeability structure of faults is highly anisotropic. The mechanisms controlling the extend of longitudinal permeability enhancement (if any), and thus producing this anisotropy are discussed in the next Section.

2.1 Fault conduit/barrier dependencies

Deformation mechanisms

Particular flow and reorientation

At low confining pressure, at burial depths of <100-200 meter (Antonellini et al. 1994), slip in unconsolidated sandstones is accommodated by particular flow and grain reorientation. That is, the rock gets disaggregated without extensive particle breaking (Fig. 3). The grain reorientation causes clay particles to align, which reduces the tortuosity in the direction of slip. This results in a small increase of the permeability in this direction with respect to the surrounding sandstone host rock (Sperrevik et al. 2002). This gives a small anisotropy in fault permeability geometry.

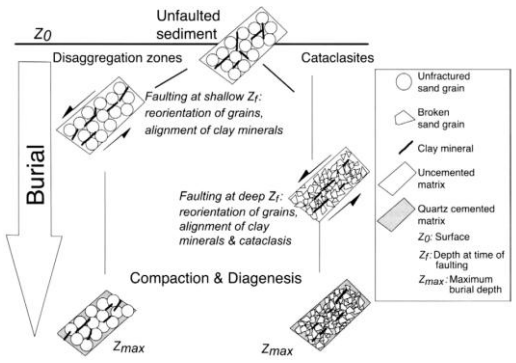

Fig. 3: Difference between cataclistic deformation where grain are broken and porosity is strongly decreased and deformation accommodated by particle reorientation (Sperrevik et al. 2002)

Cataclasis

With increasing effective stress or burial depth to ~10^3 m (Antonellini et al. 1994; discussed by Sperrevik et al. 2002), slip is accommodated by cataclasis. Grains can no longer slide along each other or rotate because the frictional forces are too high (Fig. 3). Grains are crushed and reduced, and pores collapse strongly decreasing the permeability in the core of the fault. If the clay content of the fault rock is higher, cataclasis is impeded, it is however not expected that this will yield a positive effect on permeability.

Fracturing

In strongly lithified rocks, dilatants fractures can open creating a well developed damage zone, potentially increasing the fault-parallel permeability by several orders of magnitude (Evans et al. 1997; Caine et al. 1996). First variable for effectiveness of these features is the connectivity. When the percolation threshold isn't overcome, the longitudinal permeability is still limited by the host rock porosity. Second variable is fracture aperture. Assuming flow through fractures can be modeled by laminar flow between parallel plates, the Stokes equations give a solution where the flow rate is proportional with the cube of the fracture aperture (e.g. Witherspoon et al. 1979). More open cracks thus greatly increase the hydraulic conductivity by strong fault-parallel permeability increase. Quantifying aperture of multi-oriented damage zone fractures in faults at depth is impossible. However, determining the tendency of fractures to slip and dilate in a given stress field, gives a first

order idea whether it is likely that a fault zone has high fault-parallel permeability. This is useful in the exploration phase of geothermal or petroleum related projects.

Slip tendency T_s is defined as the ratio between resolved shear stress and resolved normal stress on *some* surface (Eq.(1), Morris et al. 1996). The shear and effective normal stress acting on different surfaces depends on the orientation of the stress field with respect to those surfaces where the stress field is defined by the principle effective stresses (Jaeger et al. 2007)

$$T_s = \tau/\sigma_{neff} \geq \mu_s \quad (1$$

The shear (τ) and effective normal stress (σ_{neff}) both in Pa, can be computed, using the directional cosines of the plane's normal with respect to the principal stress axes using the known, or suspected stress field (Moeck et al. 2009). The dimensionless friction coefficient is given byμ_s . Slip tendency is a measure for whether or not slip or reactivation is likely to occur on a certain surface. Active fault zones with continuing slip show more mature damage zones with a more extensive fracture network.

The dilation of fractures is largely a function of resolved normal stress on the fracture plane, which is dependent on tectonic and lithostatic stresses and the fluid pressure. Dividing the normal stresses for different plane orientations ($\sigma_1 - \sigma_n$, Pa) by the differential stress ($\sigma_1 - \sigma_3$, Pa), yields the *dilation tendencies* T_d of those planes (Eq.(2), Moeck et al. 2009):

$$T_d = (\sigma_1 - \sigma_n)/(\sigma_1 - \sigma_3) \quad (2$$

Damage zone fracture aperture can be enhanced when their planes are oriented favorably with respect to the local stress field.

So high slip and dilation tendencies give rise to extensive and high aperture fracture networks. Off course these circumstances also give rise to seismic hazard and are conditions where hydraulic stimulation may result in strong induced seismicity. This subject is beyond the scope of this study, but is discussed in many papers (e.g. Majer et al. 2007 and Moeck et al. 2009)

Host rock: compaction and clay content

Host rock deforms by mechanical compaction with increased loading if it isn't inhibited by overpressure. Chemical compaction works by quartz cementation which can clog the host rocks pores. Extensive quartz cementation in the e.g. North Sea basin is not found until a depth of 2.5-3 km at temperatures of 90-100 °C (Bjørlykke & Egeberg 1993) and thus will play a limited role this model study, where the model basin depth is set at 3,5 km.

Generally both confining stress and temperature increase with increasing depth, decreasing the porosity and permeability of host rock significantly. Sperrevik et al. (2002) found a reasonable empirical fit between (compaction induced) permeability reduction with depth(z) in combination with variable clay V_m (%) content. The least squares planar regression (with R^2= 0.5) yields:

$$\kappa_m = 1.39 \times 10^7 e^{-(0.194V_m + 0.0043z_{max})} \quad (3$$

Fig. 4 shows the improve plot (after Sperrevik et al. 2002), with the sample data omitted, for the depth range used for the model study (see *Methods* Section). Clearly, host rock permeability is very sensitive to compaction and clay content, the maximum (V_m = 0%, z_{max}=2000 m) and minimum (V_m=40%, z_{max}=3500 m) found through this relation differ by 8 orders of magnitude. For constant clay content host rock permeabilities differ ~3 orders of magnitude (10-10^4 mD)

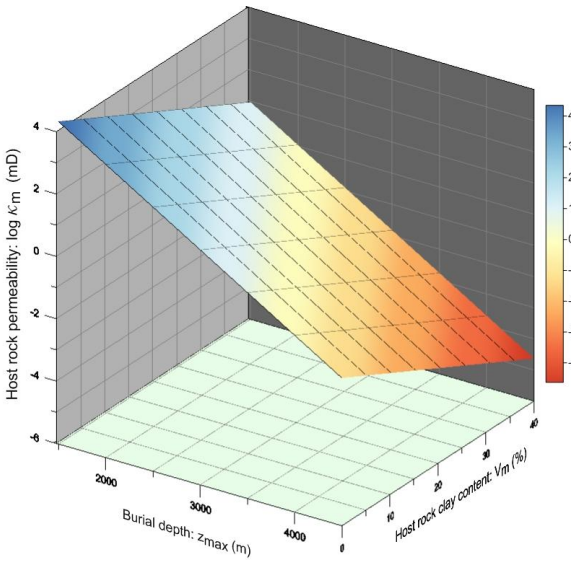

Fig. 4: Visualization of the least squares fit of the dependence of host rock permeability on burial depth and clay content (after: Sperrevik et al. 2002).

Fault zone width and geometry

When considering width, fault zones are in most studies defined as the interval where the majority of the slip is accommodated (Bense & Person 2006) which is equivalent to fault core width used in this study (after Caine et al. 1996). Here, a distinction will be made between fault core and damage zone width and their relation with fault throw and lithology. Because fractures contribute most to the permeability enhancement of a fault zone (see *Fracturing* Section), damage zone width and shape have a great influence on the conductive capabilities of a fault zone as a whole even if the fault core acts as a impenetrable seal.

Fault core width

Fault core width is dependent on the (local) throw of the fault. Successive slip events contribute cumulatively to the development of width. Another important variable is host rock lithology: clay layers tend to work as a lubricant in faults and localize the slip (Knott et al. 1996). In a sandstone-clay succession, largest widths are found where sandstone is juxtaposed upon sandstone, smallest for clay-clay juxtaposition and intermediate (and asymmetric) widths can be found at sandstone-clay contacts (Fig. 5). Field data of fault zone widths and fault throw from Sinai (Knott et al. 1996) and Northumberland (Fig. 6), where the lithology juxtapositions are known, are used to link thickness with fault throw in combination with clay content. Assigning the sandstone/sandstone and sandstone/shale regression lines a clay content fraction of 0 and 0.5 respectively, Bense & Person (2006) adapted (after Sperrevik et al. 2002) the following relation for change in fault zone width with incremental *displacement* (D) change.

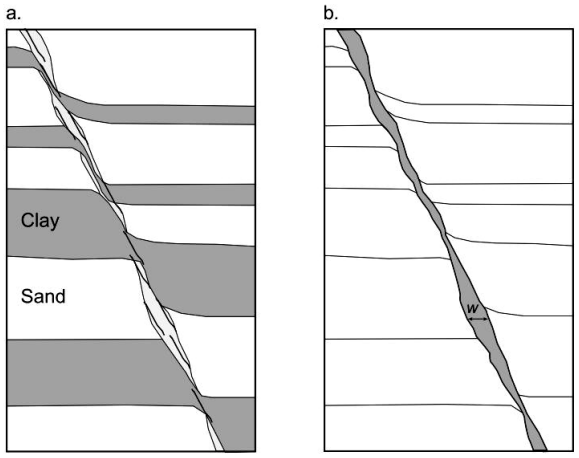

Fig. 5: Fault core width lithology dependencies. A sandstone-clay succession shows highest fault width at sand-sand, and lowest at clay-clay juxtapositions (Bense & Person 2006 after Sperrevik et al. 2002)

$$\Delta w(z) = 0.07 \cdot D \cdot e^{-0.02 V_{clay}(z)} \quad (4$$

With Δw (m) the change in fault zone width, D (m) displacement and V_{clay} the local clay content. Fault width increases with throw and is constrained by the clay content of the rock entering the fault zone with each step where contribution of the upthrown and downthrown blocks can be summed for each depth (Bense & Person 2006). This gives a good quantitative tool for variable (along fault) fault core widths with displacement.

For a 100 m displacement fault in a homogeneous lithology medium, maximum fault core thicknesses range from 7 to 2.5 meters for the used clay content spectrum. So even for large displacement, low permeable cataclistic fault rocks where the gross of the slip is accommodated are relatively thin.

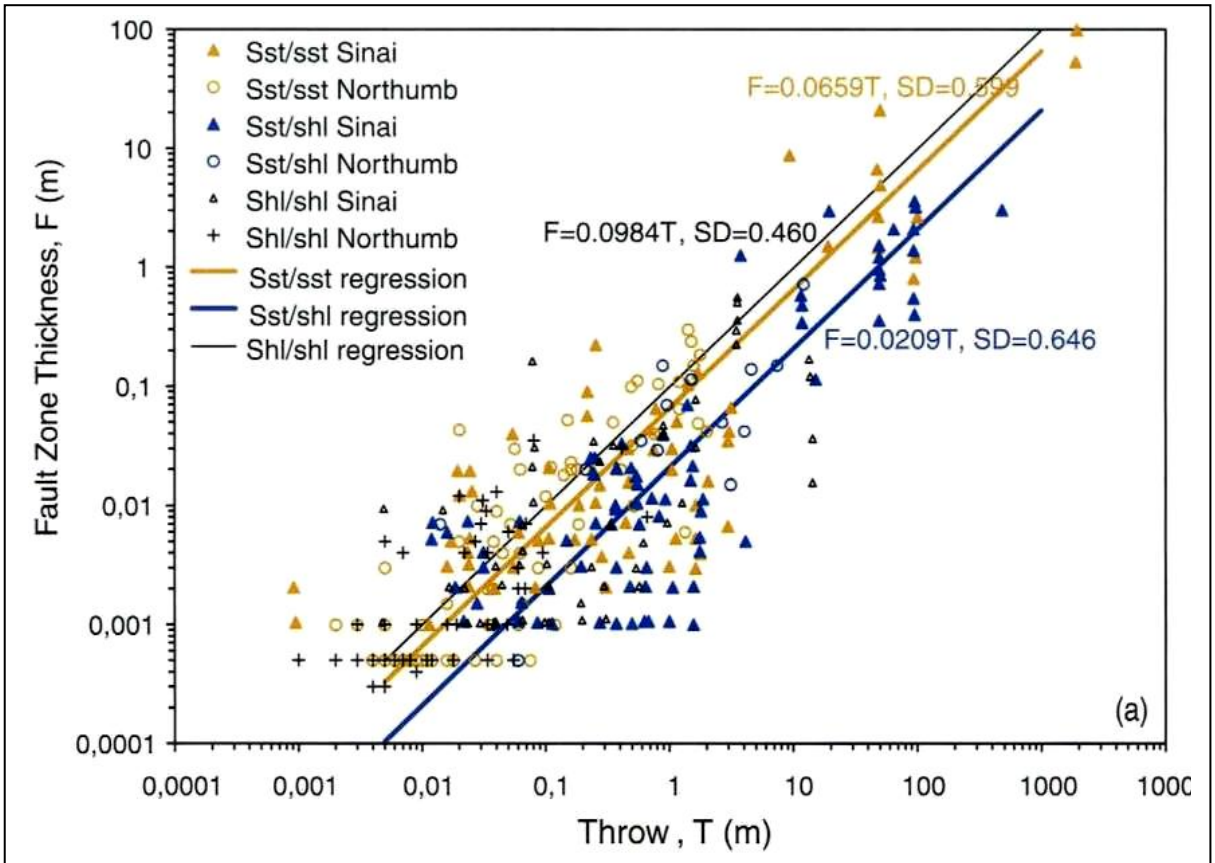

Fig. 6: Field data of fault zone thickness and throw from Sinai(Knott et al. 1996) and Northumberland(Sperrevik et al. 2002). Regression Lines for sandstone/sandstone, sandstone/shale and shale/shale contacts show the relation F(T) for the different juxtapositions (Sperrevik et al. 2002).

Damage zone width

Damage zone width is defined here as the combined hanging and footwall fracture zones flanking the fault core. Dissimilarities in symmetry between the 2 half-zones are not discussed here, though are significant (Berg & Skar 2005; Flodin & Aydin 2004).

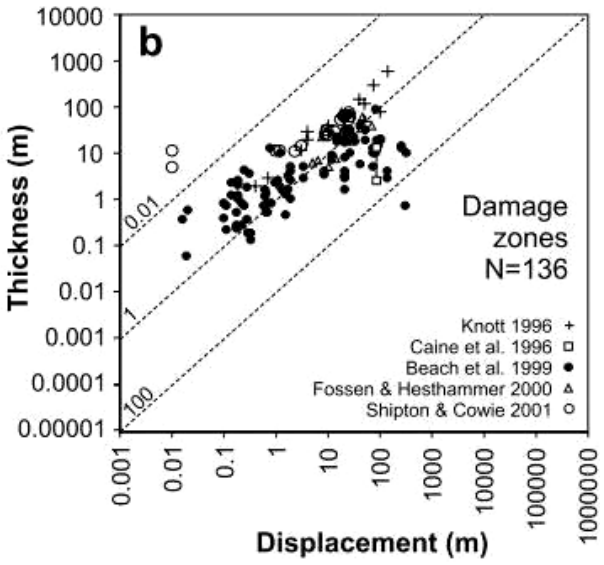

Fig. 7: Dependence of damage zone width on fault displacement for 5 data sets (after Childs et al. 2009)

Combining datasets for damage zone widths and displacement can obscure their correlation, when different damage zone definitions are used (cf. Caine et al. 1996 and Fossen & Hesthammer 2000) and potentially by clay content differences. For high host rock clay content, similar to seen in fault cores, deformation is accommodated by more ductile behavior so that fractures will not open as easily. Again, for a sandstone-clay succession this will impose damage zone "bottlenecks" in the clay-rich layers that can drastically change the overall conductive properties of the fault zone.

Positive correlations can be found by comparing similarly defined (after Caine et al. 1996) damage zones for sandstones with a known clay content (Beach & Welbon 1999; Beach et al. 1997). For low clay content sandstones Shipton et al. (2006) found from surface and drill hole data from earlier publications (2001, 2002), and in concurrence with data from (Knott et al. 1996) the following relation (R^2= 0.92):

$$w(m) = 2.5 \cdot \tau(m) + 8.5 \quad (5$$

Damage zone widths$w(m)$, found via this relation with throw $\tau(m)$ can be considered maximum values. Empirical relations with incorporation of host rock clay content have yet to be formulated, for better quantification. Regression lines for larger but potentially incomparable data sets (discussed above) indicate that the width over throw ratio comes closer to 1, but are very inconclusive (Fig. 7, Childs et al. 2009).

Damage zone geometry evolution

Slip accommodated by the fault core, can increase the strength of the fault rock by a process called local strain hardening, caused by cataclasis and interlocking of crushed grains (Faulkner et al. 2003). The stress is translated and relieved by the surrounding (host) rock when the yield strength is exceeded; this is the start of a damage zone. At a certain critical deformation density (~30%), cataclistic slip planes originate within the damage zone, which again is strain hardened. In this fashion, local slip zone strain hardening induces an ongoing widening of damage zones, were largest widths are found were fault throw is largest (Fig. 8, Shipton & Cowie 2003). This gives a first order mechanical description of the empirical relations discussed in the above Sections. The evolution of a conceptual damage zone into maturity is shown in Fig. 8 (Z.K. Shipton & Cowie 2003). With large enough ruptures over the fault as a whole, this results in a lenticular damage zone shape.

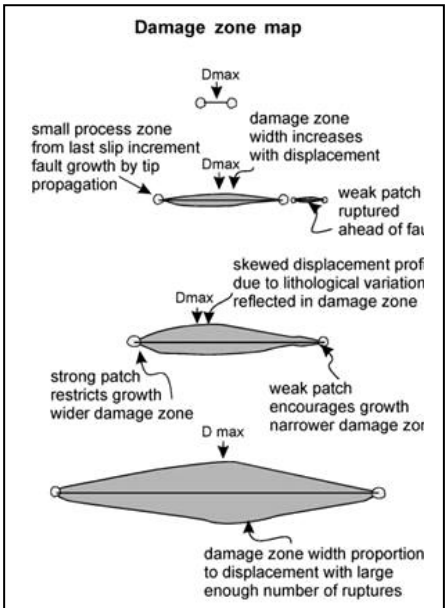

Fig. 8: Damage zone evolution with subsequent slip events (Z.K. Shipton & Cowie 2003).

2.2 Fault anisotropy estimations

In this Section, the above discussed variables will be integrated to quantify a range for permeabilities of different fault components. Using a fault that has accumulated a displacement of 150 meters in multiple slip events, fault core and damage zone widths are estimated to be 8 and 150 meters respectively. The former is calculated using an (arbitrary) clay content of 15% using Equation (4). Considering the presence of clay rich strata, for the latter a width over displacement ratio of 1 is used, which is the more conservative estimation than the factor 2.5 used in Equation (5) for clean sandstones.

Appendix 1 shows the permeability ranges found by different field studies, laboratory experiments and numerical models for the specific above mentioned conditions (Caine & Forster 1999; Aydin 2000; Flodin et al. 2001; Jourde et al. 2002). Except for (Flodin et al. 2001) all studies consider fault core material to be very fine grained resulting from ongoing cataclasis. The porosity collapse decreases their permeabilities by 4 orders of magnitude with respect to the surrounding host rock for both the fault parallel and normal directions. This implies that most high offset clastic rocks, even with a low clay content work as a seal or at least retard flow.

In the damage zone, large anisotropies occur. With respect to the host rock, the fault parallel and normal permeabilities tend to be 1 or 2 orders higher and lower respectively. Flodin et al. (2001) define a fault zone, similar to how damage zone is used here, and calculate from up-scaled field data a fault longitudinal permeability 10 times higher and fault lateral 500 times lower than that of the host rock. (Jourde et al. 2002) find 5 and 100 for these values. Aydin (2000) shows only fault normal permeabilities and argues that these can vary from 100 times lower till 10 times higher with respect to the host rock depending on the fault core deformation mechanism. Overall, fault zones tend to be sealing in the fault normal direction resulting from low fault core porosities and can be highly

conductive in the fault parallel direction resulting from permeability enhancement in the presence of fractures in the relatively wide fault damage zone.

2.3 Fault types and linking

Certain fault types and interference between faults can hold favorable conditions with respect to their permeability geometry on top of the mechanisms discussed above.

As seen in the *Deformation mechanisms* Section above, high damage zone permeabilities can only be reached when differently orientated fractures and joints have high enough tendency to dilate, breach the percolation threshold forming a well connected fracture network. These conditions are favored by an extensional tectonic stress field in normal and transtensional fault zones. On top of this, where damage zones of different faults (or segments) overlap, the development of a fracture zone is enhanced in the fault parallel direction for normal faults. When strike-slip faults are linked a pull-apart structure can develop. The extension can be accommodated by a transfer normal fault which develops a damage zone that is oriented sub-normal to the already present strike slip damage zone. Addition of both contributions results locally in a vast multi-orientated fracture network called a *linking damage zone* shown in Fig. 9 (Kim et al. 2004). The enhanced hydraulic conductivity of these systems make them good candidates for geothermal energy extraction. This is recognized but not incorporated in this model study, for simplification.

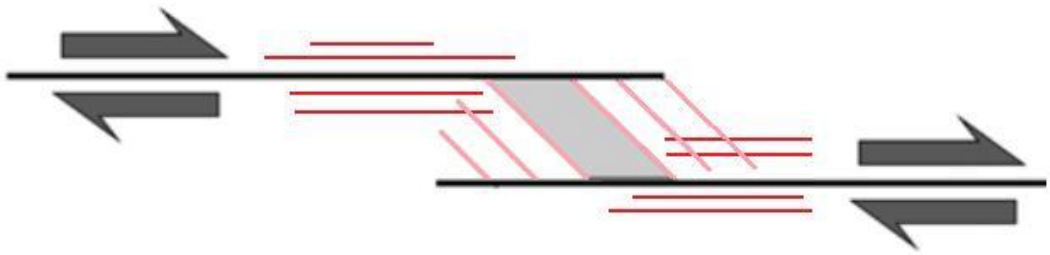

Fig. 9: Linking damage zones: intersection of the differently oriented strike-slip (red) and normal step fault (pink) damage zones results in a highly conductive permeability configuration (after Kim et al. (2004))

3. Thermal convection

As seen in the previous Section, fault zones can act as hydraulic conduits predominantly in the fault-parallel direction. Various processes can act as driving forces for fluid flow, e.g. aquifer overpressure, sediment compaction, density differences from varying salt concentrations or lateral differences in meteoric water input. In this study, only buoyant flow resulting from fluid temperature differences will be considered. This process of natural thermal convection is here defined as the sum of heat transport by conduction and advection.

First, the ability of a basin to convect as a whole will be considered under homogeneous isotropic and anisotropic permeabilities conditions and for basins consisting of different permeability layers. Second, convection within a fault zone will be investigated and third, the effect of the addition of faults to an anisotropic domain.

3.1 Basin convection

Where a vertical temperature gradient exist, heat is conducted through a porous medium and results in a linear temperature profile, the geothermal gradient, as predicted by Fourier's conduction equation. Such a system is in a state of gravitational instability because deeper higher temperature fluids that are less dense are overlain by denser fluids. Natural convection occurs as a result of this instability when the gravitational buoyant forces become larger than the viscous damping forces of the fluid. The balance of these forces is expressed in the dimensionless Rayleigh number. For the porous case this yields:

$$Ra = \frac{\rho_0 g \beta k H \Delta T}{\mu \Lambda_m} \quad (6$$

With ρ_0(kg/m^3) the reference density, g(m/s^2) the gravitational acceleration, β(K^{-1}) the thermal expansion coefficient and k(m^2) the average permeability. The temperature difference is given by ΔT(K) over domain height H(m). μ (kg/m/s) is the dynamic viscosity and Λ_m (m^2/s) the thermal diffusivity.

When the Rayleigh number reaches a critical value regular cellular flow patterns spontaneously appear and the systems starts to convect. Convection is a more effective heat transfer mechanism than pure conduction. This is quantified by Nusselt numbers at the top boundary, which is defined as the ratio of heat flow resulting from a convecting domain and the theoretical stationary conductive heat flow.

The critical Rayleigh number is dependent on the system boundary conditions and is found using linear stability analysis. Small perturbations are added to the initial conditions for the velocity, temperature and pressure fields. The governing equations described in the *Methods* Section, are then made dimensionless and are linearised between the initial state and these perturbations. The stable solutions of linearised equations, i.e. small changes in initial conditions yield small changes in final results, give critical Rayleigh numbers for a given set of boundary conditions, as well as the accompanying convection cell aspect ratios (Nield & Bejan 2006).

Isotropic permeability

For a homogeneous isotropic basin, the minimum permeability for convection to occur can be estimated for the North Sea basin height (H~3500 m) and average geothermal gradient (0.03 K/m).The critical Rayleigh number for isothermal, constant head upper- and constant heat flux, no flow lower boundaries is found to be 17.65 by Nield (1968). Including material properties and initial conditions described in the *Methods* Section using Equation (6), the critical permeability for onset of convection is found to be: $\kappa^{crit} = 2.6 \cdot 10^{-15}\,\mathrm{m}^2 = 2.6\,\mathrm{mD}$. From Bear (1988) we find this permeability to be typical for 'fresh sandstone'(Table 1) in consolidated rocks. For convection to occur the basin as a whole has to meet or exceed this critical value for these specific conditions.

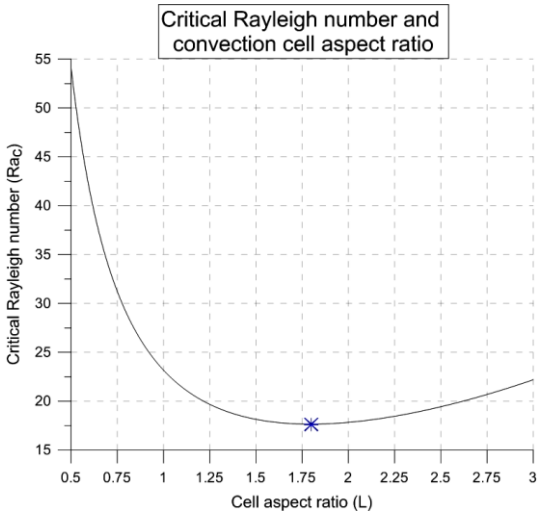

Fig. 10: Critical Rayleigh number dependence on aspect ratio for an isotropic basin. The minimum is found at L=1.8. (from McKibbin, personal communication, march 22, 2012)

Every critical Rayleigh number is associated with a wavenumber, from which the critical convection cell aspect ratio at the time of onset can be deduced. For our case, Ra_c^{min} =17.65 comes with an aspect ratio L=1.8. For H=3500 m, this means a cell width of 6650 m. When the lateral dimension of the model domain is smaller than that, onset will not occur at the minimum critical Rayleigh number. For instance, a square domain (L=1), will have a critical Rayleigh number of ~23. Critical Rayleigh number increases exponentially when the domain is 'squeezed', that is if the aspect ratio is decreased (Fig. 10). This will become increasingly more important when incorporating permeability anisotropy upon which aspect ratios increase as well.

Permeability	Pervious				Semi-Pervious				Impervious				
Consolidated rocks	Highly fractured rocks				Oil-reservoir rocks			Fresh Sandstone		Fresh Limestone, Dolomite		Fresh Granite	
$\log(\kappa)\ (m^2)$	-7	-8	-9	-10	-11	-12	-13	-14	-15	-16	-17	-18	-19
κ (mD)	10^{+8}	10^{+7}	10^{+6}	10^{+5}	10^{+4}	10^{+3}	100	10	1	0.1	10^{-2}	10^{-3}	10^{-4}

Table 1: permeability ranges for various consolidated rocks, modified after Bear (1988)

Anisotropic permeability

Critical Rayleigh numbers are found to be strongly dependent on anisotropy of permeability. McKibbin (1986) has performed linear stability analysis incorporating anisotropy ratio defined as:

$$\xi_{hr} = \left(\frac{\kappa^v}{\kappa^h}\right)_{hr} \tag{7}$$

Where κ^v and κ^h (mD) are vertical and horizontal permeabilities respectively. The subscript *hr* stands for host rock, to differentiate between basin and -later- fault (*f*) anisotropy. McKibbin (personal communication, March 22, 2012) provided a code that gives numerical solutions for critical Rayleigh numbers and cell aspect ratios for the specific set of boundary conditions used in this study were anisotropy ratio can be varied. The result of iterating over the ratio range of 1 (isotropic) to 100 is shown in Fig. 11. It is noted that critical aspect ratios are in the range 1.8-4.4 and critical Rayleigh numbers in the range of 17.65-4.13

For calculating the *system* Rayleigh number, Equation (6) has to be adapted by taking the permeability of the vertical direction. For different anisotropies, the minimum vertical permeability values and their corresponding horizontal values, required for the onset of convection are shown in Table 2. All remaining variables are kept the same as for the isotropic case so that ξ_{hr} versus κ_{hr}^{v} has the same trend as ξ_{hr} versus critical Rayleigh number in Fig. 11. From this table we can deduce that increasing the anisotropy ratio lowers the critical vertical permeability. However, the corresponding horizontal permeability needs to increases very rapidly. For example: taking χ_{hr} = 100, a vertical permeability of only 0.6 mD will result in convection, but this corresponds to a horizontal permeability of more than 60 mD for the whole basin.

ξ_{hr}	$\kappa_{hr,c}^{v}$ (mD)	$\kappa_{hr,c}^{h}$ (mD)
1	2.57	2.57
5	1.30	6.49
10	1.03	10.34
20	0.85	17.00
30	0.77	23.05
40	0.72	28.77
50	0.69	34.28
60	0.66	39.64
70	0.64	44.36
80	0.63	50.03
90	0.61	55.10
100	0.60	60.11

Table 2: Critical basin permeability

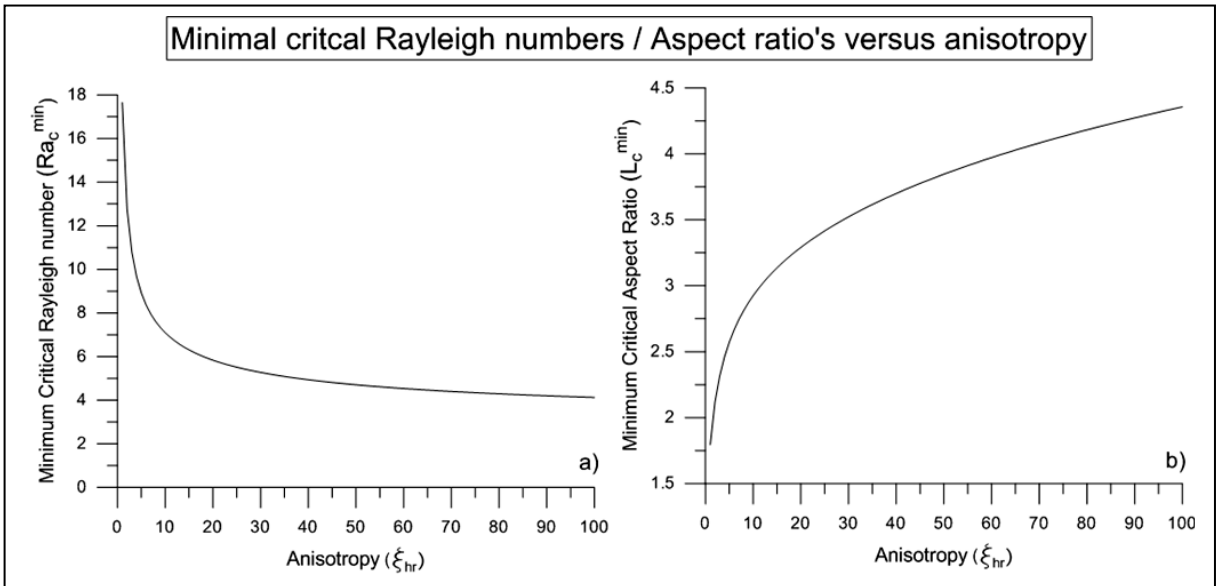

Fig. 11: Basin criticality: (a) minimum critical Rayleigh numbers for different anisotropies with (b) accompanying aspect ratios

Layered basin

A better description as compared to a homogenous permeability reservoir is a layered model where different layers have different thicknesses and permeabilities. However, for estimation of Rayleigh numbers for natural hydrothermal systems it is more convenient to use a theoretical representative homogeneous anisotropic layer. When significantly large permeability differences between individual layers exist, using an averaged whole domain permeability for finding convection properties may result in error. Very low permeability sub-layers may impede or cut off whole domain convection, and local, sub-layer convection can occur in the higher permeability strata. Mckibbin & O'Sullivan (1980) and Bjørlykke et al. (1988) investigate this effect in a 3-layer model where the central sub-layer has a contrasting permeability with respect to the surrounding rocks. The sub-layer thickness relative to the domain height (h/H) and the permeability contrast (ε) are varied (Fig. 12). The flow field streamline solutions yield the convection modes: 'whole domain' and 'local sub-layer' convection. McKibbin and O'Sullivan use thickness h/H=0.2 for all models and permeability contrast range of ε=0.01-100. Bjørlykke et al. use h/H=0.1-0.001 and ε=0.001-0.1. Compiling both computed data sets gives an overview of streamline patterns for different variable combinations and different convection modes as colored patches in Appendix 2.

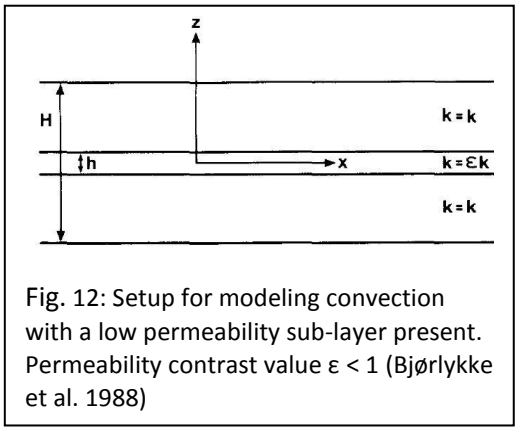

Fig. 12: Setup for modeling convection with a low permeability sub-layer present. Permeability contrast value ε < 1 (Bjørlykke et al. 1988)

Taking the North Sea basin dimensions as an example again, this yields that for a sub-layer thickness of 35 or 700 meters the permeability has to be more than 100 and 10 times smaller respectively to significantly impede flow in a 3 layer system. This implies that very significant permeability differences and thick layers are required to force a whole domain- into a layered domain convection mode (McKibbin & O'Sullivan 1980). For all cases, the critical Rayleigh number increases when introducing such a layer.

Two conditions are found not to force the transition to local convection. 1) The presence of very thin layers (sheets) with very low permeability, provided that they are not completely impermeable (McKibbin & Tyvand 1983). 2) Gradually changing permeabilities, for instance caused by porosity decrease with depth resulting from sediment compaction, can only cause whole domain convection, a smooth permeability profile is not forced into local convection systems (Gjerde & Tyvand 1984).

Modeling a layered basin with a representative homogeneous layer

Wooding (1978) found that in a system where permeability varies with depth (z-direction), for instance by layering, the average horizontal and vertical permeabilities for a basin thickness H can be found by:

$$\overline{\kappa_h} = \frac{1}{H}\int_0^H \kappa\,(z)dz, \qquad \overline{\kappa_v} = H \Big/ \int_0^H \frac{dz}{\kappa(z)} \qquad \xrightarrow{yields} \qquad \frac{\overline{\kappa_h}}{\overline{\kappa_v}} > 1 \tag{8}$$

Because the vertical component is found using the arithmetic- and the horizontal component by the harmonic mean, and the latter is always exceeds the former, finding average values always results in anisotropic permeabilities. Modeling geothermal fluid flow on basin scale using a homogeneous isotropic domain therefore inevitably results in error even when all the individual layers are assumed isotropic.

It must always be kept in mind that this analogy only holds when no thick, very low permeability layers force local convection as discussed above.

3.2 Fault convection

In-fault convection

Investigating the first order potential of thermal convection within faults can be done by determining critical Rayleigh numbers for different anisotropy ($\xi_f < 1$) vertical slabs of different thicknesses where all fault aspect ratios are: $L < 1$. For convenience, no flow boundary conditions with isothermal upper and (higher temperature) lower bounds are used, for which analytical solutions exist (modified after Epherre 1975).

$$Ra_c(L) = \frac{\pi^2(\xi + L^2)(1 + L^2)}{\xi L^2} \quad (9$$

When the domain allows for a range of aspect ratios; when the 'fault' is significantly wide, the critical Rayleigh numbers are the minima of Equation (9) for different anisotropies, found by differentiating with respect to L. This yields:

$$L_c^{min} = (\xi)^{-1/4} \quad \xrightarrow{yields} \quad Ra_c^{min} = \pi^2 \left[1 + \sqrt{1/\xi}\right]^2 \quad (10$$

In Fig. 13a the critical Rayleigh numbers for aspect ratios L=0.05-0.1-0.2 are shown for the anisotropy range ξ=0.001-1. For comparison, the minimum critical Rayleigh numbers are plotted, that are found at different aspect ratios for different anisotropies (Fig. 13a,b). Equivalent critical vertical permeability values can be found using the right Y-axis. Conversion using Equation (6) is performed with the same parameters as in the previous Section again, only the domain thickness (H) has to be replaced by fault height (H_f). The equivalent permeabilities are shown for a vertical fault of 1500 meters. For the range of aspect ratios chosen this means fault widths of 75, 150 and 300 meters respectively.

Results of the analytical solutions for the simplified fault model with forced aspect ratios yield:

- For very high anisotropy faults (ξ= 0.001) critical Rayleigh numbers, even the minimum value, all exceed 10^4, so no convection will occur below the equivalent vertical permeability of 3400 mD.
- For the whole anisotropy range an L=0.05 requires more than 1350 mD vertical permeability for onset of convection.
- Critical vertical permeabilities for L=0.1 at ξ= 0.01 and 0.1 are 680 and 370 mD
- Critical vertical permeabilities for L=0.2 at ξ= 0.01 and 0.1 are 440 and 120 mD

A more realistic model that approaches the permeability structures as described in the *Fault zone architecture and permeabilities* Section yields changes in critical Rayleigh numbers. The following qualitative remarks can be made about (1) fault cores (2) damage zone geometry (3) complex boundary conditions:

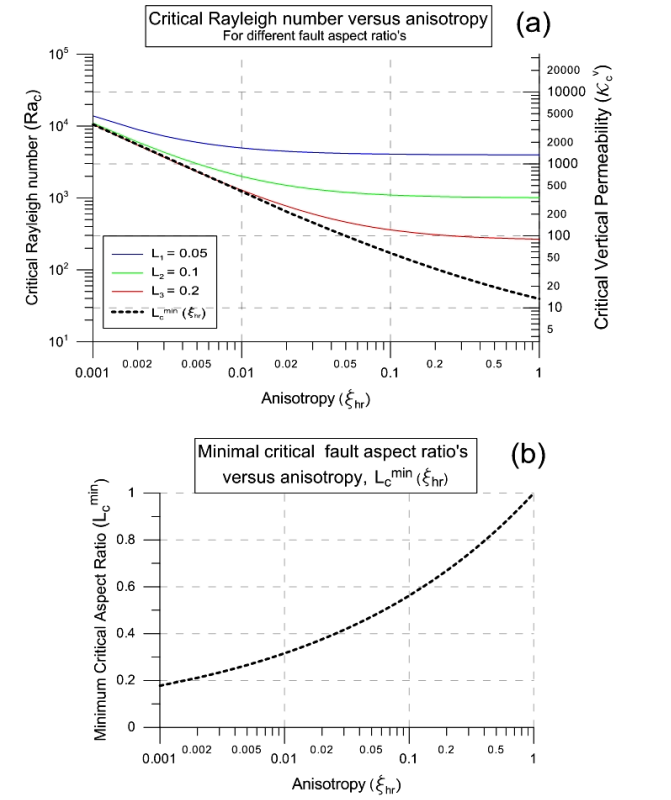

Fig. 13: Criticality of in-fault convection. (a) critical Rayleigh numbers and equivalent vertical fault permeabilities related to fault anisotropies for different imposed fault aspect ratios. Included are the critical values for the minimal (optimal) aspect ratio that is shown in (b) to be a function of anisotropy as well.

Fault cores in most cases are found to be sealing in the lateral direction as discussed in the *Fault zone architecture and permeabilities* Section. So a fault core acts as a strong convection cell divider. If footwall and hanging wall half damage zones are two separate flow domains, convection is forced in half the aspect ratios, so critical Rayleigh numbers increase (Fig. 13, cf. L=0.2 and L=0.1).

In the Fault zone width and geometry Section and Fig. 8 we found that a mature damage zone has a lenticular shaped permeability structure. The effect of this geometry on critical Rayleigh numbers is difficult to quantify, but an increase is expected as narrowing towards the fault tips may yield an energetically unfavorable forced increase in fluid vorticity.

Instead of no flow boundaries used here, faults are found to be enveloped by a layered or averaged anisotropic (Equation (8)) medium. These very complex flow boundaries where there is a sharp transition in anisotropy direction (ξ_{fault} <1, ξ_{hr} >1) make predictions for system critical Rayleigh numbers rather difficult if even possible. 'Open' flow boundaries tend to lower critical Rayleigh numbers as the adjacent host rock can accommodate some of the flow depending on the specific absolute permeabilities. This effect is found by Mckibbin (1986) for 2 vertical slabs with different , however homogeneous *and* isotropic, permeabilities.

So for onset of convection within fault zones to occur, high displacements are needed to create wide and permeable enough fault zones. Fault cores and lens-shaped damage zones may impede -, and 'open' boundary conditions my enhance convection with respect to the conditions used in the simple fault model. The analytical solutions therefore may present an under- as well as an overestimation of the equivalent fault-parallel permeabilities needed for in-fault convection.

Basin with faults

Finding system Rayleigh numbers for anisotropic basin containing 'inverse' anisotropy fault(s) cannot be done in a predictive way. Though (McKibbin 1986b) discusses a simplified case where he considers a square, isotropic permeability domain that envelops a thin vertical slab ('fault') of variable thickness with a higher, but also isotropic permeability than the surrounding host rock (i.e. ε <1). The Rayleigh number for the models is increases until super-criticality is reached and the central slab starts convecting in-fault. Upon increasing the permeability of the thin stratum a sudden transition occurs. Flow through the fault becomes unidirectional upward *or* downward and the return flow is accommodated by the surrounding medium. The transition is reflected in surface heat-flow by the local Nusselt numbers. In the former case a step change is seen but the latter shows a positive anomaly (or negative for downward unidirectional flow) of the heat-flux directly above the fault (Fig. 14(a))The transition point is also found to be a function of fault width, were for thinner faults a smaller permeability contrast with the host rock is required. However, the relation between transition point, fault width and permeability contrast isn't quantified. If it was it would have been only for his specific set of boundary conditions and square domain dimensions.

In Fig. 14(b) Mckibbin (1986) arbitrarily places 2 vertical higher permeable slabs in the same domain. It is evident that the most favorable convection cell configuration is that of unidirectional flow through the narrow faults where one fault shows up- and one down flow. McKibbin doesn't elaborate on this model set up, but uses it as an example. Interesting results might be obtained when extending this model by varying fault widths, permeability contrasts and spacing between the faults in a horizontally wider domain, to allow for more aspect ratio convection cells.

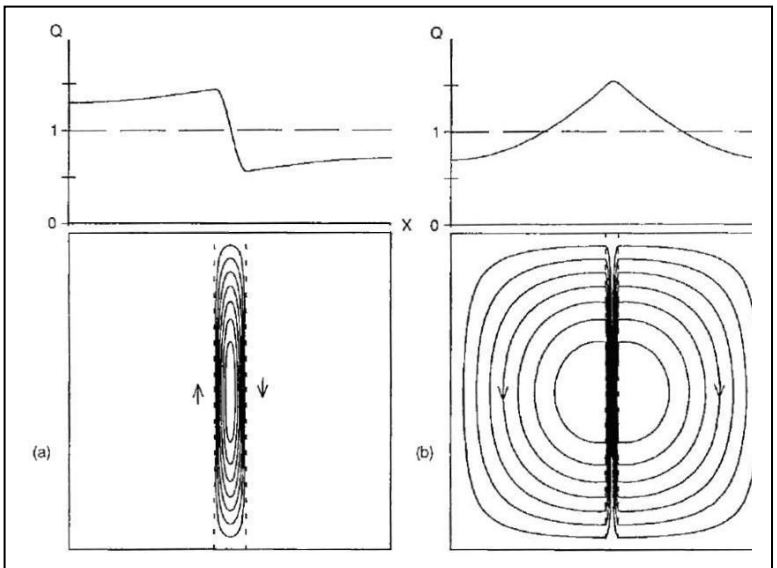

Fig. 14(a): Streamline patterns and local Nusselt numbers for a system enveloping a vertical high isotropic permeability stratum with permeability contrast ε=100 and relative 'fault' width (a) h/H=0.1 and (b) h/H=0.04 (McKibbin 1986a)

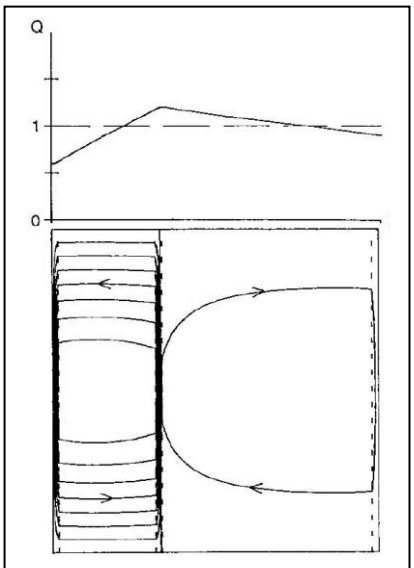

Fig. 14(b): As in (a), but with 2 faults with ε=100 and h/H=0.1 (McKibbin 1986a)

4. Methods

Here, the methods used for the finite element flow and heat transport model study using FEFLOW are described. Material properties and their dependencies on especially temperature are discussed. An analytical description is provided, including approximations and assumptions. The model description Section gives an overview of the used geometries, initial and boundary conditions, as well as meshing and temporal properties.

4.1 Material properties

Mechanical properties

Permeability ranges

The model equivalent of the North Sea basin is considered, using a homogeneous permeability in this study. For convenience, the effect of compaction on permeability with depth is neglected. From Equation (3) also displayed in Fig. 4, taking the average basin depth of 1750 m and using a clay content 25-35%, a basin permeability range of about 10-50 mD is found, used as maximum values here. From Equation (8) we find that, averaging over different permeability strata *has to* result in anisotropy. Simms et al. (2004) and Fleming et al. (1998) use basin anisotropies of ξ_{hr}=10 and 100 respectively. These values are taken as a range in this study, so that minimum vertical basin permeabilities are in the range of 0.1-2 mD (see Table 3).

From the various results discussed in the *2.2 Fault* anisotropy estimations Section summarized in Appendix 1, fault-parallel permeabilities are found to be 1 or 2 orders of magnitude higher than the maximum (horizontal) host rock permeability. For the lateral direction this is 1 or 2 orders *lower*. So in this study, a range of 100-500 mD is mostly used (some 1500+ mD faults are investigated) for fault-parallel permeabilities with anisotropy value 100 or 1000.

Property	(Reference) Value	Unit
κ_{hr}^{h}	10-50	mD
κ_{hr}^{h}	0.1-2	mD
ξ_{hr}	10-100	-
κ_{f}^{L}	10-500	mD
κ_{f}^{T}	0.3-5	mD
ξ_{f}	10^2 or 10^3	-
φ	0.2	-
S_0	0.0001	m^{-1}
$\alpha_{L,T}$	5, 0.5	m
T_0	10	°C
$\rho_0^f(T_0)$	999.7	kg/m^3
$\mu_0^f(T_0)$	$1.26 \cdot 10^{-3}$	kg/m/s
$\rho^f C^f$	$4.2 \cdot 10^6$	$J/m^3/K$
$\rho^s C^s$	$2.52 \cdot 10^6$	$J/m^3/K$
λ^f	0.65	W/m/K
λ^s	3.0	W/m/K
λ_m	2.53	W/m/K
Λ_m	$6.17 \cdot 10^{-7}$	m^2/s

Table 3: model input (reference) variables

Other properties

Estimations for some properties are very hard to obtain for a basin as a whole. For porosity a conservative value of 0.2 was chosen. Thermal conductivity is dependent on porosity, this is described below. Basin specific storage- as well as thermal dispersivity values are almost impossible to obtain with the goal of representing a heterogeneous layered basin in a homogeneous model. So the values are arbitrarily chosen to be 0.0001 m^{-1} for specific storage and 5 and 0.5 m for longitudinal and transversal thermal dispersivity respectively (Table 3).

Temperature dependent fluid properties

Density and Thermal expansion coefficient

Density variation is the key parameter for buoyancy driven convective flow. The state equation for fluid density ρ^f (kg/m^3) when no solute concentration differences exist and fluid is considered incompressible is given by:

$$\rho^f(T) = \rho_0^f e^{-\beta(T)(T-T_0)} \approx \rho_0^f [\,1 - \beta(T)(T - T_0)] \quad (11$$

With ρ_0^f the reference density value at T_0 (°C). Over a large range of temperatures, expansion coefficient $\beta(T)$ (K^{-1}) is a function of temperature, and so can't be considered a constant for geothermal problems.

Diersch (2005) uses experimental data, where fresh water is heated from 0 to 150 degrees Celsius. The resulting density curve is fitted with a sixth order polynomial, shown in Fig. 15 with its coefficients.

$$\rho^f(T) = a + bT + cT^2 + dT^3 + eT^4 + fT^5 + gT^6 \quad (12$$

Using this fit (R=1), reference density ρ_0^f can be determined by choosing an initial condition reference temperatureT_0. A Taylor series expansion for ρ^f can be performed around this reference temperature (Diersch 2005, Eq. 1-88) using the polynomial expression to gain an expression for the temperature dependent thermal expansion function $\beta(T)$, which can be used in state Equation (15) containing model reference values.

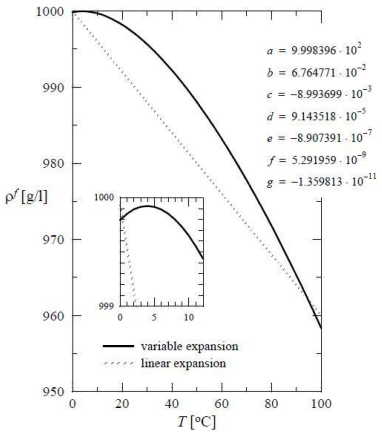

Fig. 15: Density dependence on temperature: (dotted line) linear expansion (bold line) measured density change with temperature fitted by a 6th order polynomial, and it's coefficients a-g (Diersch 2005)

Viscosity

Again, when solute concentration differences aren't considered, dynamic fluid viscosity μ^f (kg/m/s) is solely a function of temperature, which variations are significant for geothermal processes. Mercer & Pinder (1974) give an empirical relation for fresh water:

$$\frac{1}{\mu^f(T)} = \frac{1+0.7063\zeta-0.04832\zeta^3}{\mu_0^f} \quad \text{with} \quad \zeta = \frac{(T-150)}{100} \quad (13$$

The reference viscosity $\overline{\mu_0^f}$ in this constitutive equation is taken at T=150°C. To get an expression using a custom reference viscosity μ_0^f for initial condition reference temperature T_0 a viscosity relation function f_μ can be defined (Diersch 2005):

$$f_\mu = \frac{\mu_0^f}{\mu^f(T)} = \frac{1 + 0.7063\zeta - 0.04832\zeta^3}{1 + 0.7063\zeta_{(T=T_0)} - 0.04832\zeta^3_{(T=T_0)}} \quad (14$$

Constant properties

Concerning heat properties, volumetric heat capacity and thermal conductivity are assumed constant in FEFLOW. Below 200 °C, the specific heat capacity for water increases with temperature. Density is found to have an inverse dependency to this on temperature. The model input parameter volumetric heat capacity is found by multiplication of these 2 fluid variables which results in an almost constant value over a large range of temperatures.

Thermal conductivity is slightly temperature dependent for the fluid phase, but hardly for the solid phase. When the conductivities of the different phases are similar, the effective thermal conductivity is given by:

$$\lambda_m = \varphi\lambda^f(T) + (1 - \varphi)\lambda^s \quad (15$$

Where λ_m (W/m/K) is the effective thermal conductivity, λ^f and λ^s (W/m/K) represent the thermal conductivities for the fluid and the solid phase and porosity is denoted by φ(-)

Since porosity for a basin as a whole is unlikely to be >0.3, the value for λ^s has the highest weight for effective thermal conduction so that the weak temperature dependence for the fluid phase can be neglected.

From these properties the effective thermal diffusivity can be derived, which is used in determining system Rayleigh numbers.

$$\Lambda_m = \frac{\lambda_m}{(\rho C_p)^f} \quad (16$$

Here Λ_m (m^2/s) and λ_m (W/m/K) are the effective values for thermal diffusivity and medium conductivity and $(\rho C_p)^f$ (J/m^3/K) gives the volumetric heat capacity for the fluid phase.

Though all these properties are close to temperature independent, thermal diffusivity is still a function of porosity, because a change in porosity shifts the value for the effective conductivityλ_m. So system Rayleigh numbers (Eq. (6)) are sensitive to porosity changes while critical Rayleigh numbers are not. With higher conduction, heat diffuses more easily and a system becomes more stable (or less critical). The inverse holds for volumetric heat capacity.

Input values for the discussed properties can again be found in Table 3.

4.2 Analytical description

In this Section the governing equations for thermally variable density flow are presented. Thermal buoyancy is taken as the controlling driving force. Contributions of salt concentration, sediment compaction, tectonic deformation, regional topography and meteoric influx are disregarded.

For modeling coupled fluid and heat transport, the conservation of mass and momentum have to be considered in combination with the conservation of energy.

The conservation of mass of a fluid in a saturated porous medium with no sources or sinks terms is given by (after Diersch 2005):

$$S_0 \frac{\partial h}{\partial t} = \nabla \cdot \left(\boldsymbol{K} \left(\nabla \mathrm{h} + \frac{\rho^f - {\rho_0}^f}{{\rho_0}^f \mathrm{g}} \hat{\mathrm{e}}_\mathrm{z} \right) \right) + \mathrm{Q_{EB}(T)} \tag{17}$$

Where S_0 (m^{-1}) is the system specific storage resulting from fluid (small) and solid phase compressibility, h(m) hydraulic head and $\hat{\mathrm{e}}_\mathrm{z}$ is the unit vector in the z-direction (Fig. 16). The Extended Oberbeck-Boussinesq Approximation term is given by $\mathrm{Q_{EB}(T)}$, described below.

$\boldsymbol{K}$(m/s) is the hydraulic conductivity tensor that is constructed using the state equation for density and the constitutive equation for viscosity given in the previous Section:

$$\boldsymbol{K} = \frac{\boldsymbol{k} \rho^f \mathrm{g}}{\mu^f} \tag{18}$$

Here $\boldsymbol{k}$ (m^2) represents the intrinsic permeability tensor.

Conservation of momentum is represented by Darcy's Law that is derived from the Navier-Stokes equations by homogenization under the assumptions that:

- Kinetic energy can be ignored, this implies that fluid movement is limited to laminar flow, which is often the case when not forced but only natural convection flow problems are considered (Nield & Bejan 2006)
- Discharge is controlled by average properties, so valid only for macroscopic scale problems
- Fluid properties have to be constant, which obviously is not the case for the strong temperature dependencies. This limitation is avoided by using *equivalent fresh water* head h_f. That is, hydraulic heads are calculated using reference density $\rho_0(T_0)$ so that driving gradients can be determined for different density heads. It must be kept in mind that h_f is a theoretically introduced parameter that cannot be measured directly (Holzbecher 2005). For convenience, the subscript f is omitted in this paper.

This yields:

$$\vec{q}^{\,f} = -\boldsymbol{K} (\nabla h + \frac{\rho - \rho_0}{\rho_0 \mathrm{g}} \hat{\mathrm{e}}_\mathrm{z}) \tag{19}$$

With $\vec{q}^{\,f}$(m/s) being the specific discharge or Darcy velocity.

Conservation of thermal energy where no heat sources or sinks are present is given by the heat transport equation with a conductive and advective (1st and 2nd term between parentheses respectively) part:

$$(\rho C)^m \frac{\partial T}{\partial t} = \nabla \cdot \left(\boldsymbol{\lambda} \nabla T - \rho^f C^f \vec{q}^f T\right) \quad (20$$

Here $(\rho C)^m$ (J/m^3/K) is the medium volumetric heat capacity and λ (W/m/K) the thermal conductivity.

Extended Oberbeck-Boussinesq Approximation

For most flow problems where no large density differences occur in the fluid, the Oberbeck-Boussinesq approximation can be used. In those cases it is assumed that density differences are significantly small to be neglected in al terms of the flow equation except in the buoyancy term in the momentum equation (Darcy's law).

FEFLOW has the option to extend this approximation by incorporating mass-dependent and temperature-dependent compression effects by the insertion of a sink/source term $\mathrm{Q_{EB}(T)}$ in the conservation of mass equation (Eq. 1-110, Diersch 2005). This option is used in the model study.

4.3 Model description

In this model study a fully saturated fresh water porous medium with transient fluid flow and heat transport is simulated in a 2D vertical projection, where fluid viscosities and densities are taken as temperature dependent as described above.

Model geometry

The geometry of the model domain is depicted in Fig. 16. The height of the domain is chosen to be H=3.5 km approximately corresponding to depth of the North Sea basin. The lateral dimension of the domain L=31.5 km = 9 ·H. This high width is chosen to avoid limitation of aspect ratio for convecting cells as described in the Thermal convection Section.

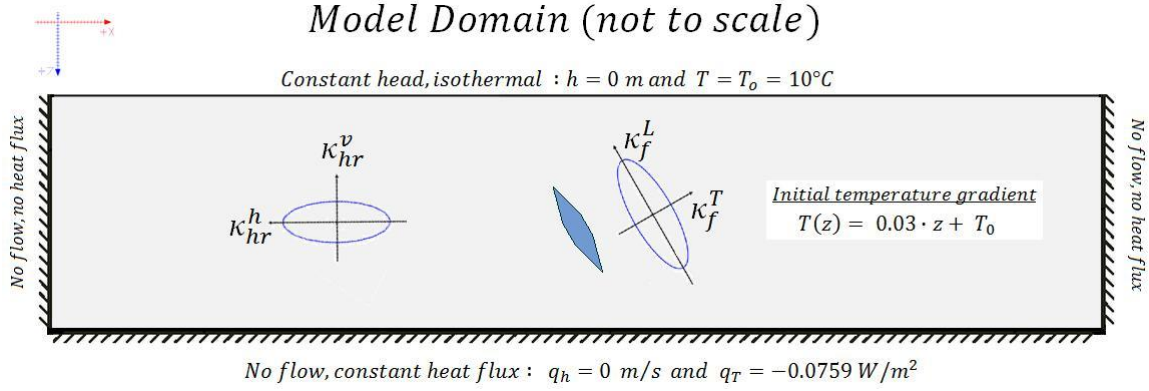

Fig. 16: Model domain with initial temperature gradient, boundary conditions and qualitative images of fault and host rock anisotropy ellipse orientations.

For different model runs, one or multiple faults are inserted which have lenticular shapes with a maximum width of 150 or 300 m and a length of 1500 m. A simplified fault model is used, where damage zone permeability is taken to be homogeneous but anisotropic (see *Mechanical properties* Section) and to avoid meshing difficulties a fault core is left out. The faults are positioned far away from the boundaries so that fault-tip/host rock dynamics can be investigated. All faults have a dipping angle of 60° unless otherwise specified. 4 different configurations that are used and their corresponding codes are in shown in Fig. 17. The number that precedes the configuration code indicates the spacing between the centers of the fault zones where 2,4 and 8 give the spacing L/2,L/4 and L/8 as fractions of the length of the model domain, these correspond to 15.8, 7.9 and 3.9 km apart respectively.

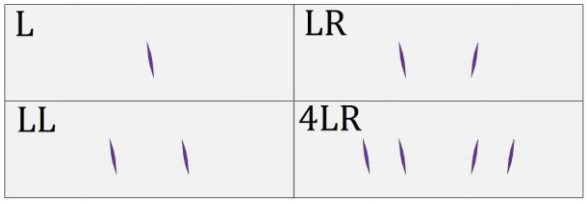

Fig. 17: Applied fault model configurations For multiple fault models, fault spacings were varied by ~16, 8 and 4 kilometers (vertical exaggeration x3)

Initial and Boundary conditions

Initial condition for the velocity field is that of a standing static fluid, i.e. q^f=0. The initial temperature field is a set to a typical geothermal gradient, as found for the North Sea basin:

$$T(z) = 0.03 \cdot z + T_0 \quad (21$$

With z (m) the depth direction and T_0(°C) being the reference temperature (Table 3)

Flow boundaries are set to 'no flow' except for the upper boundary which is open to water flux at constant head. This could indicate a stationary water table or the interface between groundwater and sea water. The no flow lower boundary represents the underlying impermeable basement rocks.

Thermal boundary conditions for the side boundaries are set to be thermally insulating, that is no heat flow. The lower and upper boundaries are set to be of constant heat flow q_H^f (W/m^2) and isothermal T_0 respectively. The value for the heat flow boundary is set to maintain the pre-set geothermal gradient (0.03 K/m) when no thermal convection takes place and is derived by multiplication of the effective thermal conductivity (Table 3) with this gradient. An isothermal top might result from significantly faster mixing of air above the water table or ocean currents at the seafloor, with respect to heat flows through the porous basin.

Boundary conditions are similar to other basin model studies (Fleming et al. 1998; Simms & Garven 2004) and are summarized in Fig. 16.

Meshing and temporal settings

Because the anisotropy directions of the host rock and the faults are almost perpendicular to each other, strong mesh refinement has to be done at the fault/host rock interfaces and especially at the fault tips. The models are discretized using an average of $1.3 \cdot 10^5$ elements in a triangular mesh to allow for irregular (lenticular) fault shapes. Average host rock element size is h ~100 meter and ~10 meter for fault material. Smallest elements ~5 m are placed at the above mentioned interfaces, where gradients are expected to be highest. Smooth gradual transitions are applied as can be seen in Fig. 18. To maximize stability and accuracy, spatial descretization errors have to be kept at a minimum. The main criterion for this is gird-Péclet criterion for heat transport (Diersch & Kolditz 2002).

$$Pe = \frac{\left\|\vec{q}^f\right\| h}{\Lambda_m} \leq 2 \quad (22$$

With $\left\|\vec{q}^f\right\|$ (m/s) being the magnitude of the Darcy velocity, h (m) the characteristic element size and Λ_m (m^2/s) the effective thermal diffusivity.

FEFLOW has an automatic time-step control feature, which predicts the behavior of the system and adjusts the time-step accordingly. However, probably as a result of the strong acceleration at onset of convection, the solutions overshoots, introducing non-physical instabilities. The solution is fully biased within 1 time step, which can't be restored by reducing the time step in the next iteration. We

even find oscillating convection cells resulting from over and undershooting by too coarse time steps. To control the temporal descretization errors, the maximum time step is set so that the Courant criterion is never violated (Diersch & Kolditz 2002):

$$Cr = \left\|\vec{q}^{\,f}\right\| \frac{\Delta t_{max}}{h} \leq 1 \qquad (23$$

With Δt_{max} (s), being the maximum time step.

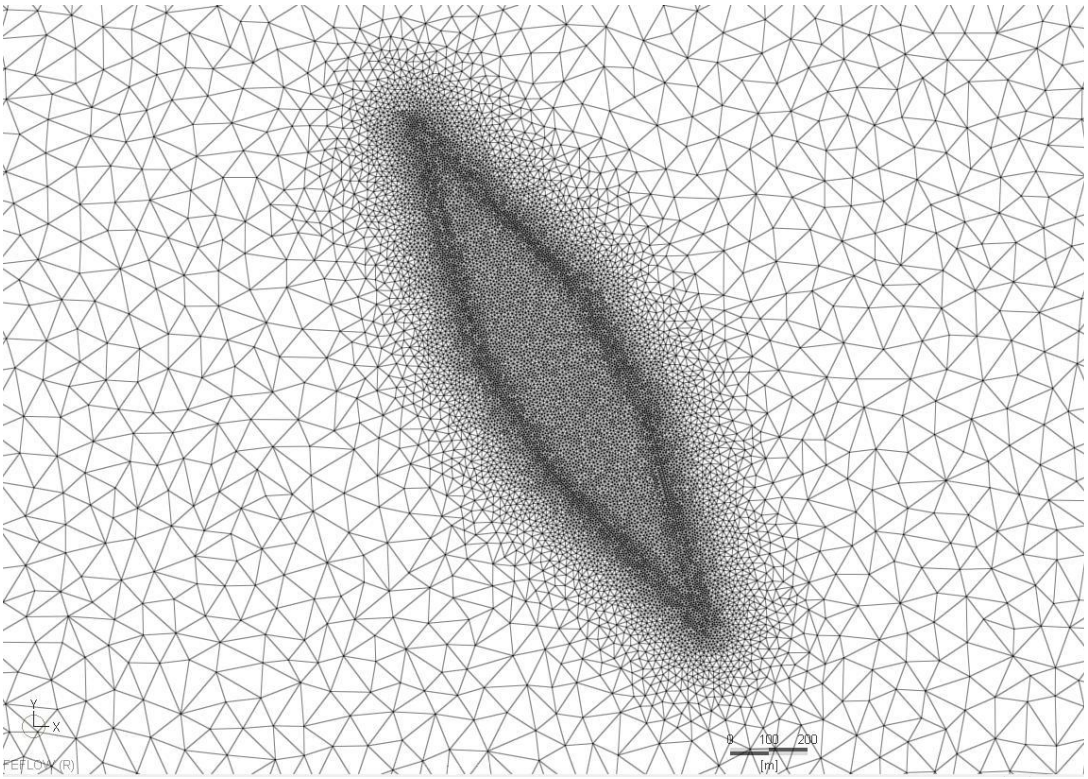

Fig. 18: Mesh refinement around fault zone. Element dimensions: host rock h~100 m, fault zone h~10 m, interfaces host rock/fault zone and at fault tips h~5 m

5. Results

All results are depicted in Appendix 3, where comparison between different variable models is shown by two figures. The top figure shows the (model) surface heat flow normalized by the heat flow for a purely conductive system (0.759 W/m^2). This gives the local Nusselt numbers along the surface. Upon integration it was found that all upper boundary (total) Nusselt numbers are close to one, which indicates that only laminar flow takes place. The bottom figure shows depth deviation of the 70°C isotherm which runs through the centre of the fault zones for a purely conducting case. For most models, these 2 figures show the same trends depending on amplitude and wavelength of the anomalies. For some models the local Nusselt number figure is omitted to allow for comparison when large differences for isotherm anomalies exist. The isotherm figures are deduced from temperature distribution plots for the whole domain of which an example is depicted in Fig. 19(discussed below).

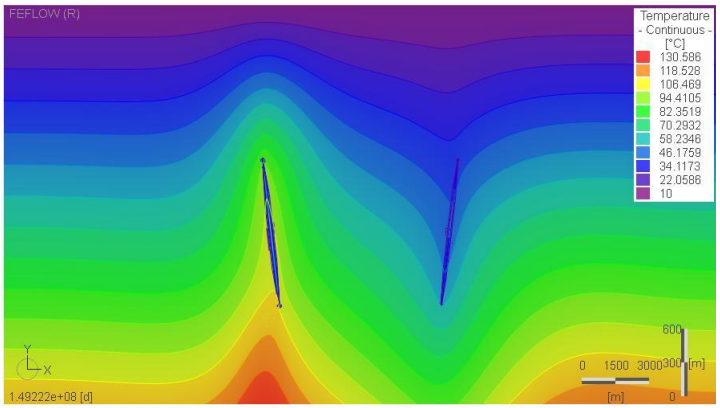

Fig. 19: Example of whole domain temperature distribution for the same case as seen in Appendix 3(h). Asymmetry of the isotherm anomalies resulting from along-fault advective flow is clearly visible in this high horizontal basin- (κ_{hr}^{h} = 30 mD) and fault-parallel (κ_{f}^{L} = 500 mD) permeability model.

5.1 Natural basin convection

In the *Anisotropic permeability* part of the *Thermal convection* Section, it was pointed out that critical Rayleigh values for whole domain convection without presence of faults, are a function of the anisotropy of permeability. So the choice of anisotropy factor and absolute value of horizontal (maximum) permeability are the main factors that determine if a model will start to convect when thermal expansion, basin thickness, initial temperature gradient and thermal diffusivity are kept constant. Table 4 shows the different used basin permeabilities and how close each of these systems is to criticality for onset ($\mathrm{Ra}/\mathrm{Ra}_c$, cf. Table 2). Higher reservoir permeability increases the Rayleigh value and higher anisotropies lower the *critical* Rayleigh number. The 2 chosen permeability combinations, for which criticality could be reached are both at the high end (horizontal 50/20 mD combined with vertical 2 mD) of the used permeability spectrum. Onset times for the 2 supercritical cases however, were found to exceed 3.65·10^9 days (10 Myr). A time span over which a sedimentary basin might not be considered steady state anymore with respect to permeabilities, porosities etc. In this study onset time is defined as the moment when a thermal anomaly occurs. Therefore, whole basin convection wasn't considered to be a relevant research focus even for supercritical basins.

ξ_{hr}	κ_{hr}^{v} (mD)	κ_{hr}^{h} (mD)	$\mathrm{Ra}/\mathrm{Ra}_c$
10	10	1	0.85
10	20	2	**1.70**
15	10	0.67	0.66
20	10	0.5	0.55
20	15	0.75	0.82
25	50	2	**2.34**
50	30	0.6	0.85
100	10	0.1	0.16
100	20	0.2	0.33
100	25	0.25	0.41
100	30	0.3	0.49
100	50	0.5	0.82

Table 4: System criticality for used basin model permeabilities

5.2 Single central fault zone

For 1 fault zone arbitrarily dipping 60 degrees enveloped by a porous basin, all models (figure a) show a depression of the 70°C isotherm at the location of the fault as a result of buoyant down flow. The return upflow is accommodated by the basin porosity and creates 2 bulges left and right to the depression. Faster downward fluid flow is allowed by the system when increasing the horizontal permeability of the reservoir. Then, a greater portion of the length of the basin is used because of the higher conductivity, so that the relatively small vertical permeability of the reservoir is a less limiting factor. This is expressed by broader bulges where the isotherm deviation stays positive even at the domain wall (>15 km distance).

For extremely high longitudinal fault permeabilities (2500 mD is ~5 larger than predicted maximum (*4.1* Material properties *Section*) shows an instable temporal tendency for in-fault convective circulation, which is expressed as a step change in isotherm, which disappears with time and again an isotherm depression originates.

5.3 Double fault systems

Equal orientation (LL4)

2 fault zones spaced by 0.25 times the domain length (~7.9 km) show significant in-fault convection only for extreme longitudinal fault permeabilities in figure (b). The wavelength of the isotherm anomalies are so small that the local Nusselt number graph at the upper boundary shows no difference when the permeability is halved, whereas the isotherm deviation is decreased by an order of magnitude (from 10 to 1 m). In-fault circulation again is only found at small times (t_1~10^5 days with ~10^{-4} m/d). When increasing time to 50*t_1 the systems evolves to a similar system as observed in the last Section, but with 2 isotherm depressions at the fault zones locations.

Figure (c), shows the effect of changing the longitudinal fault permeability κ_f^L within physically reasonable range of 50-400 mD for fault anisotropy ξ_f=100 at t=3.65·10^8 d (1 Myr). The reservoir is equal for all models with κ_{hr}^h=10 and κ_{hr}^v=0.5 mD. Similar to the trend in the previous Section, for lower fault permeabilities two isotherm depressions occur. When increasing to higher permeabilities, the amplitudes increases but one becomes dominant over the other and the trend becomes more and more asymmetric. For the higher part of the permeability range it can be seen that the isotherm is lowered for one of the faults and raised for the other, the latter being caused by buoyant upwelling resulting in thermal convection. Convective circulation cells are in these cases found to be bound by the fault zones.

Also interesting to note is that the asymmetric depression profile of the 100 mD model is mirrored with respect to the other models, indicating that clockwise as well as anti-clockwise *tendencies* can develop.

When letting the lower fault permeability models run a factor 4 times longer in figure (d), full convective circulation develops for 100 mD and even for 50 mD (clockwise) upon increasing the duration another 1.8 times. Though, over runtimes of >10^9 days (10 Myr), fault zones aren't considered to be steady-state systems with respect to their conductive properties in this study, the models do show that the start of fault bound convection is a function of time, but develops faster with higher longitudinal fault permeabilities κ_f^L.

In figure (e), when decreasing the reservoir anisotropy ξ_{hr}= 20 to 10 (so becomes κ_{hr}^{v}=1 mD), vertical flow through the basin is easier so that thermal advection through faults becomes more effective. Already at half the time (t_2 =1.85·10^8 days) compared to figure (c), isotherm elevation amplitudes are 4-10 times higher. At 3.65·10^8 days, the 100 mD fault zone with anisotropy ξ_f=10 (not shown) gives an order of magnitude larger isotherm deviation and convective circulation start, but it was found to have a lower velocity upflow (2.5·10^{-5} m/d) compared to down flow (2.4·10^{-4} m/d**)**

Fault width is another variable used in this graph. Halving the fault zone width (f_w =300 to 150 m) and doubling the permeability (κ_f^L =100 to 200 mD) gives comparable results. This observation confirms the findings of Fleming et al. (1998). The profiles are however mirrored indicating again that anti- as well as clockwise circulation tendencies can occur.

Both above mentioned permeability combinations have a below critical Rayleigh number with respect to the basin itself (0.55 and 0.85 respectively). All occurring thermal convection is due to the presence of faults that locally increase Rayleigh numbers.

Reversed orientation (LR4)

In figure (f), for a two fault system where the dips are in opposite directions, increasing the longitudinal fault permeability κ_f^L= 400 to 500 mD *and* increasing the vertical reservoir permeability κ_{hr}^{v}= 0.67 to 1 (i.e. ξ_{hr}= 15 to 10) shows only small differences at small times (3.65·10^7 days) in the 2 downward isotherm anomalies.

However in figure (g), increasing κ_{hr}^{h} to 50 and κ_{hr}^{v} to 2 mD shows already an order of magnitude higher anomalies at a third (1.22·10^7 days) of the runtime for (f). This permeability combination falls in the region of supercritical Rayleigh numbers (Ra/Ra_c = 2.34) and thus the whole system would convect eventually. Later times could not be displayed for this model because the accelerating fluid velocities made the model unable to meet the Courant criterion. However, domain convection is not expected to occur before 10^9 days, so that all convection can still be attributed to the presence of faults.

Figure (h) shows the evolution of thermal convection in a high κ_{hr}^{h}=30 mD and κ_f^L =500 mD model through time. The graph looks similar to figure (c) where the fault permeability was the variable, but here the same model is show at multiple times. At 1.22·10^7, the 2 depressions in the 70°C isotherm can (just) be seen. At 8.55·10^7, the left fault zone starts to accommodate thermal upflow which progresses more and more with time, until the positive and negative anomaly are approximately of the same size (500-600 m) at ~10^8 days and convection is fully developed.

Variable orientation (LL8 and LR8)

Comparison of the 2 orientations studied above while keeping all other variables constant in figure (i), shows (at 2 times) that 2 fault zones dipping toward each other is the more effective configuration for convective circulation than 2 dipping in the same direction. The developing isotherm anomalies are a factor 2 larger for the former. Both of these configurations can be seen to be very effective with respect to what we have seen so far. This seems to be associated with their small distance from each other.

Fault spacing (LR2 and LR4)

In figure (j), for spacing comparison there is a small data gap. The LR2 and LR4 models are run under the same conditions with $\kappa_{hr}^{h/v}$=10/0.67 and $\kappa_{f}^{L/T}$= 400/4. However, the compared LR8 model is run with $\kappa_{hr}^{h/v}$=15/0.6 and $\kappa_{f}^{L/T}$= 300/0.3. These models are obviously not equal but can to a first order be compared to investigate the spacing effect. However, it must be kept in mind that κ_{hr}^{h} is a sensitive parameter as found in the *4 fault zones* Section below.

Continuing, for $t_1 = 1.43 \cdot 10^8$ days, the LR2 configuration shows significantly higher amplitudes of (negative) isotherm deviation then the LR2 version, but shows little development to a circulation loop. The LR4 configuration is already strongly in asymmetry at that time whereas the LR2 spacing shows only slight asymmetry even when time progresses to $3.65 \cdot 10^8$ ($2.5 * t_1$). The LR8 spacing is clearly the most effective. Closer spaced fault zones develop circulation very fast (onset ~$6 \cdot 10^7$ days) and can change the local temperature distribution significantly, as also seen in the previous Section and also in the simplified models in the *Basin with faults* part of the *Thermal convection* Section.

Fault dipping angle (LL8 at 60° and 45°)

Shallowing the fault dip in figure (k) is expected to have a negative effect on its potential heat transport in the vertical direction. For instance, for a very shallow 10° dipping fault, the horizontal permeability of the host rock gets enhanced locally because it almost coincides with the high fault-parallel permeability, but the vertical permeability might become even less then the basin value as a result of the high anisotropy of fault permeability. Comparing 60 and 45 degree fault zones shows a dramatic effect: the difference in relative isotherm elevation is 2 orders of magnitude.

Also, in Fig. 19 the effect of an inclined fault on the whole domain temperature distribution can clearly be seen. Heat is transported by thermal *advection* in the fault-parallel direction, resulting in an asymmetric temperature distribution over each fault. This effect is observed in all models where significant thermal advection is present, but is not investigated in this study.

5.4 Multi fault systems

4 or 2 fault zones

We see that in figure (l), 2 sets of fault zones spaced L/8 between each other and L/4 between the 2 sets is a more effective configuration for thermal convection then any of the 2 fault zone sets so far. Onset of convective circulation is reached in the shortest time span (<$5 \cdot 10^7$ d, not shown). For high κ_{hr}^{h} =30 mD, a 2 fault LR4 configuration reaches similar amplitudes as a 4 fault system when the runtime is doubled. For figure (m), comparison with L/8 spacings (LR8 and LL8 from the *Variable orientation* Section) makes sense because the multi fault models are essentially 2 LL8 half models stuck together. However, the two sets strongly affect each other and enhance the convective circulation, so that relative isotherm deviations are a factor 2-3 higher for the 4-fault system.

4 fault zones

The multi fault figure (n) contains 3 different models with the same configuration and fault properties. The horizontal permeability is stepwise increased (κ_{hr}^{h}=10, 15, 30 mD) together with the anisotropy resulting in a decreasing (κ_{hr}^{v}=1, 0.75, 0.67 mD) vertical permeability. The figure clearly shows that circulation effectiveness is very sensitive to horizontal permeability even when vertical reservoir permeability is decreased.

6. Discussion

6.1 Basin and Fault model parameters

Basin

This model study uses an equivalent homogeneous anisotropic medium to model a layered heterogeneous sedimentary basin. From the *3.1 Basin* convection Section we find that the anisotropy approximation is reasonable when permeability is considered variable with depth (Equation (8)). However when permeability contrasts get significantly high (Appendix 2), whole basin convection is impeded and a transition takes place to local interlayer convection, if criticality can still be reached. In this study it is assumed that layer permeability contrasts lay below that transition threshold and that no significant lateral heterogeneity is present. Both assumptions are not necessarily true, but have to be made when detailed stratification geometry is unknown.

On top of layering, permeability decreases with depth and time as a result of sediment compaction (Equation (3), Sperrevik et al. 2002). The model doesn't incorporate this effect, but permeability values are based on the average burial depth. This approximation can be made, provided that changes are gradual. Smooth permeability changes with depth, will not induce a transition to local convection (Gjerde & Tyvand 1984). Temporal changes in permeability resulting from compaction may induce upward fluid flow, this effect is disregarded.

Hydraulic conductivity values resulting from the depth independent permeability yield that fluid velocities are underestimated for above average depth and overestimated at greater depth. This results from the increase of temperature with depth and the subsequent decrease of temperature dependent viscosity. This effect yields unrealistic fluid velocities, at depth to high and shallow to low. On the other hand, for the North Sea basin Bjørlykke (1994) states that their exist a salinity stratification. For increasing concentration with depth the viscosity increases as well. This opposes the effect of viscosity decrease with increasing temperatures.

To what extend these effects cancel each other with respect to resulting conductivity will have to be quantified. This depends on the concentration profile, geothermal gradient and the choice of constitutive equation. Still, I propose using a temperature independent viscosity when only fresh water and a depth independent permeability is used, to get a more realistic fluid velocity field.

The presence of salinity stratification also opposes the effect of temperature changes on density and thus can decreases gravitational instability of the system. This might impede the onset of convection.

Fault zones

With respect to permeability, fault zones where modeled without a fault core and with a wide, homogeneous but anisotropic lenticular shaped damage zone. This configuration is assumed to be constant with time.

Fault cores where omitted to avoid meshing problems for very small features (<10 m). For all models it was observed that with high anisotropy values, lateral fault flow is negligible with respect to the fault-parallel velocities. So discarding a fault core didn't result in significant changes.

For a wide damage zone to develop in nature, the fault core has to be subject to strain hardening upon deformation, so that a significant part of the stress relief has to be accommodated by fracturing of the adjacent (damage) zone and is not localized in the core. This adds the conditions that the main deformation mechanism in the damage zone is fracturing and cataclasis in the fault core. This will only be the case when the fault intersects host rock that is strongly lithified, and fault core rock doesn't incorporate high amounts of clay or evaporates that work as lubricants. Else, strain would be localized in the fault core and no damage zone would develop.

Though the permeability structure is known to be heterogeneous, the anisotropy assumption (with $\kappa_f^L > \kappa_f^T$) is justified by the fact that most fractures in the damage zone are sub-parallel. However, the fracture density will decrease with distance from the fault zone which is not incorporated in this fault zone model.

The lenticular shape for the fault permeability geometry is based upon the relation between damage zone width and local displacement (Fig. 8) which is largest at the center of the core and smallest at the fault tips. This is under the assumption that the intersected host rock is homogeneous with respect to its deformation mode. In clay rich strata, as seen above, deformation is strongly localized and the narrow damage zone that forms will be partially clogged with clay, decreasing its permeability in that layer. In an alteration of sandstones and clays, this will result in permeability 'bottlenecks' in the clay layers (cf. Fig. 5 for fault cores). This might impose a very significant error when representing a layered system fault, using a homogeneous case lenticular permeability geometry. Unfortunately, for unknown stratification or fundamental basin convection research, such an assumption has to be made.

In an alteration of sandstone with impermeable but *strongly lithified* layers, for instance limestone instead of clay, a very permeable damage zone might originate. This might allow for thermal convection if the cells are fault bound even if these strata have a high enough permeability contrast to impede whole domain convection in an *otherwise critical basin without fault zon*es (see *Basin* Section)

Whether or not the steady-state approximation for permeability geometry is valid or not is not easily quantified. Upon subsequent slip events, fault zones can become higher in permeability over time and heterogeneity may change as well. An opposing effect may come from mineralization or crack healing when faults are inactive for a period of time. For this model study positive and negative effects on fault permeability have to be assumed to be in equilibrium.

6.2 Model results

As read in the *Thermal convection* Section, convection can occur in a gravitational unstable system, when the gravitational buoyant forces become larger than the viscous damping forces of the fluid. This originates in randomly developing local density instabilities that with *time* progressively become larger until the whole system becomes unstable and circulation starts.

The presence of faults increases the amplitude of the random local density instabilities that initially would die out. This can decrease the onset time of a system that already exceeds its critical Rayleigh number and can even bring sub-critical basin systems to convect as seen in the model results. Another favorable condition is that (sub-vertical) faults and host rock have opposing anisotropy, so a high conductivity circuit exists, running through the faults and across the fault tips.

Sensitive onset parameters

All models initially show downward flow, where cold dens water forms a 'finger' in the high permeability fault zone(s), where the amplitude of the resulting negative temperature anomaly is found to be strongly dependent on fault-parallel permeability (κ_f^L) and fault width. The return flow is accommodated by host rock permeability. For multi-fault models this *can* progress to an asymmetric profile, where the difference between the amplitude of the thermal anomalies at the different faults becomes progressively larger. This results from fluid flow acceleration in one of the faults and deceleration in the other. Such systems eventually develop full convective fluid circulation, where the down flow is accommodated by one of the fault zones and the return flow by the other. If circulation develops, and within what time frame is found to be strongly dependent on spacing between the faults and horizontal host rock permeability (κ_{hr}^h). This is because higher κ_{hr}^h allow for easier horizontal flow in the host rock and can thus be considered as a relative spacing decreaser. High permeability and broad fault zones result in large amplitudes for the temperature anomalies but are not the determining factors for onset of convection.

Figure (j) shows a remarkable result. At t=1.43·10^8 days a faults spacing of L/2~16 km shows a factor 2 larger anomaly amplitudes than L/4~8 km spaced faults for the same conditions, no explanation is found for this difference. These results are overshadowed by the anomalies resulting from the already fully developed convection of the L/8~4 km model. The most effective convection is expected to be found at a spacing that is closest to the critical aspect ratio of the host rock. From (Fig. 11) we find that for ξ_{hr}=15, this ratio is 3.14. This implies a convection cell width of ~4.7 km for fault height 1500 m which is closest to the L/4 configuration. As the presence of fault zones results in a local change in the *effective* vertical basin permeability, aspect ratios might decrease.

More research is required to find the detailed effects of spacing, by using longer time spans and/or higher κ_{hr}^h values for more different fault spacings.

In-fault convection

Only for very high (>1500 mD) fault permeabilities, fluid was found to be convecting within a fault. The accompanying very local thermal anomalies are of such short wavelengths that no contribution to the surface heat flow was detected. Also, the in-fault flow configuration was unstable for my models and transition to downward fingering occurred at short times. More realistic fault zones also

have a fault core that often times works as a seal for especially fault-transversal flow. This would compartmentalize the in-fault flow domain, so that it gets narrowed into 2 sub domains. This will make in-fault flow even less likely because the convection cell aspect ratio is forced to decrease which increases its critical Rayleigh number.

Circulation direction

Simms & Garven (2004) state that the circulation direction of a convection cell that is bounded by 2 inclined faults dipping in the same direction (here: LL configuration), is determined by whether the basin is in a critical or sub-critical condition. In this study it was found that both clockwise and anticlockwise convection occurs under sub-critical basin Rayleigh numbers. A clear example is displayed in appendix 3(d), which for the combination of anisotropy ξ_h=20 with horizontal host rock permeability κ_{hr}^{h}=10 mD yields a $\mathrm{Ra}/\mathrm{Ra}_c$=0.55 value (Table 4), which far below critical.

Fault angle

The effect of fault angle was on onset of convection was also investigated by (Simms & Garven 2004). The found that dip-shallowing to 45° doesn't have a large effect. Though, it is expected to impede convection to some extent, only 1 model was run to investigate fault dip effects, so the result depicted in appendix 3(k) is probably erroneous and might have to be discarded.

7. Conclusions

7.1 Literature study

Fault zone architecture and permeability structure

It is found that fault zones can be highly conductive to fluid flow in the fault-parallel direction. Where lateral flow is impeded by the low permeability, fine grained fault core, longitudinal fault flow occurs through the adjacent damage zone. The permeability anisotropy of such damage zones is quantified to be in the range of ξ_f= 10^2-10^4 (Appendix 1). A wide permeable damage zone can develop under the following conditions. (1) The fault core is *strain hardened* upon deformation, so that stress is translated to the adjacent host rock. (2) That intersected host rock must be strongly lithified so that stress relief after the yield strength of the rock is exceeded will result in fracturing, and not in grain size reduction that will reduce permeability. When this condition is met, higher fault offset result in a vaster fracture network. (3) The fractures must be oriented favorably to the regional preferentially extensional stress field to allow them to be sufficiently open for fluid flow.

Clay rich or evaporate layers don't meet these requirements. Fault cores deform by localized smearing so that translated stresses are small. On top of this, damage zone fractures don't develop or are clogged in clay-rich layers. So when considering the hydraulic properties of a fault as a whole in an alteration of sandstone and clay layers, the clay damage zones form less wide and less permeable bottlenecks to flow.

Thermal convection

To model large-scale convective flow in a basin that has permeabilities that vary with depth, it is found that averaging to obtain an equivalent homogeneous domain always results in anisotropy

(Equation(8)). However, local convection may occur when low permeability strata act as a flow regime dividers. This will only occur if the layers are significantly thick and have a very high permeability contrast with respect to the surrounding rock (Appendix 1).

In-fault convection is found to be very difficult by using the analytical solutions for a simplified fault model. This results from the increase in critical Rayleigh number upon forcing convection to occur in very narrow aspect ratios. Also, it is shown that a fault core acts as flow regime divider, so that aspect ratio are forced another factor 2 lower. Translating these results into a more realistic model with varying fault width is thought to increase Rayleigh number even more. In-fault convection therefore will only occur for very high permeability and/or very wide faults.

7.2 Model results

All models initially show cold downward dens fingers at the fault locations and return flow is accommodated by the basin porosity. Transition to fault bound convection cells is primarily a function of the spacing between the faults and the horizontal host rock permeability. Longitudinal fault permeability and fault width are associated with larger temperature anomaly amplitudes. Onset times are found to be a function of all of the above parameters.

So, especially where fault zones are spaced close together in a sedimentary basins and the effect of permeability bottlenecks in clay-rich layers isn't too large, higher temperatures at shallower depths can be found above fault zones. This might be used as an advantage for finding preferential locations for *Enhanced Geothermal Systems.* The higher temperature at shallower depth and the high permeability structure of faults will limit drilling costs and enhance extraction rates.

8. Acknowledgements

I would like to thank Prof. dr. Ruud J. Schotting as my academic supervisor and Guus Willemsen, Nick Buik and Noortje Heijnen as supervisors at IF-technology. Additionally I would like to thank dr. Amir Raoof for his modeling support. Special thanks goes to Prof. Robert McKibbin who provided me with a code for calculating critical Rayleigh numbers and convection cell aspect ratios for my specific set of boundary conditions.

9. References

Antonellini, M., Aydin, A. & Bridge, D., 1994. Effect of Faulting on Fluid Flow in Porous Sandstones: Petrophysical Properties 1. *AAPG Bulletin*, 78(3), pp.355–377.

Ates, A., Bilim, F. & Buyuksarac, A., 2005. Curie Point Depth Investigation of Central Anatolia, Turkey. *Pure and Applied Geophysics*, 162(2), pp.357–371.

Aydin, A., 2000. Fractures , faults , and hydrocarbon entrapment , migration and flow. *Marine and Petroleum Geology*, 17(2000), pp.797–814.

Beach, A. et al., 1997. Characteristics of fault zones in sandstones from NW England: application to fault transmissibility. *Geological Society, London, Special Publications*, 124(1), pp.315–324.

Beach, A. & Welbon, A.I., 1999. Reservoir damage around faults; outcrop examples from the Suez Rift. *Petroleum Geoscience*, 18(3), pp.109–116.

Bear, J., 1988. *Dynamics of Fluids in Porous Media*, Dover Publications Inc.

Bense, V.F. & Person, M.A., 2006. Faults as conduit-barrier systems to fluid flow in siliciclastic sedimentary aquifers. *Water Resources Research*, 42(5), pp.1–18.

Berg, S.S. & Skar, T., 2005. Controls on damage zone asymmetry of a normal fault zone: outcrop analyses of a segment of the Moab fault, SE Utah. *Journal of Structural Geology*, 27(10), pp.1803–1822.

Bjørlykke, K., 1994. Fluid-flow processes and diagenesis in sedimentary basins. *Geological Society, London, Special Publications*, 78(1), pp.127–140.

Bjørlykke, K. & Egeberg, P.K., 1993. Quartz Cementation in Sedimentary Basins. *AAPG Bulletin*, 77(1993), pp.1538–1548.

Bjørlykke, K., Mo, A. & Palm, E., 1988. Modelling of thermal convection in sedimentary basins and its relevance to diagenetic reactions. *Marine and Petroleum Geology*, 5, pp.338–351.

Bredehoeft, J.D., Belitz, K. & Sharp-Hansen, S., 1992. The hydrodynamics of the Big Horn Basin: A study of the role of faults. *AAPG bulletin*, 76(4), pp.530–546.

Caine, J.S., Evans, J.P. & Forster, C.B., 1996. Fault zone architecture and permeability structure. *Geology*, 24, pp.1025–1028.

Caine, J.S. & Forster, C.B., 1999. Fault zone architecture and fluid flow: Insights from field data and numerical modeling. *Geophysical monograph*, 113, pp.101–127.

Chester, F.M. & Logan, J.M., 1987. Composite planar fabric of gouge from the Punchbowl fault, California. *Journal of Structural Geology*, 9(5-6), pp.621–634.

Childs, C. et al., 2009. A geometric model of fault zone and fault rock thickness variations. *Journal of Structural Geology*, 31(2), pp.117–127.

Diersch, H.-J.G., 2005. FEFLOW finite element subsurface flow and transport simulation system. *Reference manual*, (Berlin, Germany: WASY GmbH, 2005).

Diersch, H.-J.G. & Kolditz, O., 2002. Variable-density flow and transport in porous media: approaches and challenges. *Advances in Water Resources*, 25(8-12), pp.899–944.

Epherre, J.F., 1975. Critère dápparition de la convection naturelle dans une couche poreuse anisotrope. *Revue Génerale de Thermique*, 14, pp.949–950.

Evans, J.P., Forster, C.B. & Goddard, J.V., 1997. Permeability of fault-related rocks, and implications for hydraulic structure of fault zones. *Journal of Structural Geology*, 19(11), pp.1393–1404.

Faulkner, D.R., Lewis, A.C. & Rutter, E.H., 2003. On the internal structure and mechanics of large strike-slip fault zones: field observations of the Carboneras fault in southeastern Spain. *Tectonophysics*, 367(3-4), pp.235–251.

Fleming, C.G., Couples, G.D. & Haszeldine, R.S., 1998. Thermal effects of fluid flow in steep fault zones. *Geological Society, London, Special Publications*, 147(1), pp.217–229.

Flodin, E.A. et al., 2001. Representation of Fault Zone Permeability in Reservoir Flow Models. *Proceedings of SPE Annual Technical Conference and Exhibition*, pp.1–10.

Flodin, E.A. & Aydin, A., 2004. Faults with asymmetric damage zones in sandstone, Valley of Fire State Park, southern Nevada. *Journal of Structural Geology*, 26(5), pp.983–988.

Fossen, H. & Hesthammer, J., 2000. Possible absence of small faults in the Gullfaks Field, northern North Sea: implications for downscaling of faults in some porous sandstones. *Journal of Structural Geology*, 22, pp.851–863.

Gjerde, K.M. & Tyvand, P.A., 1984. Thermal convection in a porous medium with continuous periodic stratification. *International Journal of Heat and Mass Transfer*, 27(12), pp.2289–2295.

Holzbecher, E., 2005. Free and forced convection in porous media open at the top. *Heat and Mass Transfer*, 41(7), pp.606–614.

Jaeger, J.C., Cook, N.G.W. & Zimmerman, R.W., 2007. *Fundamentals of rock mechanics*, fourth ed. Blackwell Publishing, Oxford, UK.

Jourde, H. et al., 2002. Computing permeability of fault zones in eolian sandstone from outcrop measurements. *AAPG bulletin*, 86(7), pp.1187–1200.

Kim, Y., Peacock, D.C.. & Sanderson, D.J., 2004. Fault damage zones. *Journal of Structural Geology*, 26(3), pp.503–517.

Knott, S.D. et al., 1996. Spatial and mechanical controls on normal fault populations. *Journal of Structural Geology*, 18, pp.359–372.

Majer, E.L. et al., 2007. Induced seismicity associated with Enhanced Geothermal Systems. *Geothermics*, 36(3), pp.185–222.

McKenna, J.R. & Blackwell, D.D., 2004. Numerical modeling of transient Basin and Range extensional geothermal systems. *Geothermics*, 33(4), pp.457–476.

McKibbin, R., 1986a. Heat Transfer in a Vertically-Layered Porous Medium Heated from Below. *Transport in Porous Media*, 1, pp.361–370.

McKibbin, R., 1986b. Thermal convection in a porous layer: Effects of anisotropy and surface boundary conditions. *Transport in Porous Media*, 1, pp.271–292.

McKibbin, R. & O'Sullivan, M.J., 1980. Onset of convection in a layered porous medium heated from below. *Journal of Fluid Mechanics*, 96(02), pp.375–393.

McKibbin, R. & Tyvand, P.A., 1983. Thermal convection in a prous medium composed of alternating thick and thin layers. *International Journal of Heat and Mass Transfer*, 26, pp.761–780.

Mercer, J.W. & Pinder, G.F., 1974. Finite element analysis of hydrothermal systems. In J. T. Oden et al., ed. *Proceedings of International Symposium on Finite-Element Methods in Flow Problems*. UAH Press, pp. 410–414.

Moeck, I., Kwiatek, G. & Zimmermann, G., 2009. Slip tendency analysis, fault reactivation potential and induced seismicity in a deep geothermal reservoir. *Journal of Structural Geology*, 31(10), pp.1174–1182.

Morris, A., Ferrill, D.A. & Henderson, D.B., 1996. Slip-tendency analysis and fault reactivation. *Geology*, 24(3), pp.275–278.

Mozley, P.S. & Goodwin, L.B., 1995. Patterns of cementation along a Cenozoic normal fault: A record of paleoflow orientations. *Geology*, 23(6), pp.539–542.

Nield, D.A., 1968. Onset of Thermohaline Convection in a Porous Medium. *Water Resources Research*, 4(3).

Nield, D.A. & Bejan, A., 2006. *Convection in Porous Media* 3rd ed., Springer, New York (1999).

Schill, E., Geiermann, J. & Kümmritz, J., 2010. 2-D Magnetotellurics and Gravity at the Geothermal Site at Soultz-sous-Forêts. In *Proceedings World Geothermal Congress 2010*. Bali, Indonesia, 25-29 April 2010.

Shipton, Z.K. & Cowie, P.A., 2003. A conceptual model for the origin of fault damage zone structures in high-porosity sandstone. *Journal of Structural Geology*, 25(3), pp.333–344.

Shipton, Zoe K et al., 2006. How Thick is a Fault? Fault Displacement-Thickness Scaling Revisited . *In Abercrombie, R. (Eds) Earthquakes: Radiated Energy and the Physics of Faulting*, AGU, pp.193–198.

Simms, M.A. & Garven, G., 2004. Thermal convection in faulted extensional sedimentary basins: theoretical results from finite-element modeling. *Geofluids*, 4, pp.109–130.

Sperrevik, S. et al., 2002. Empirical estimation of fault rock properties. *Norwegian Petroleum Society Special Publications*, 11, pp.109–125.

Tester, T.W. et al., 2006. The Future of Geothermal Energy. *An assessment by an MIT-led interdisciplinary panel*.

Willemsen, G., Heller, R. & Van Wees, J.D., 2011. Diepe geothermie 2050; Een visie voor 20% duurzame energie voor Nederland.

Witherspoon, P.A. et al., 1979. Validity of cubic law for fluid flow in a deformable rock fracture. *Water Resources Research*, 16(6), pp.1016–1024.

Wooding, R.A., 1978. Large-scale geothermal field parameters and convection theory. *New Zealand Journal of Science*, 27, pp.219–228.

10. Nomenclature

Symbol	Unit	Description
C^f and C^s	J/K/kg	Specific heat capacity
Cr	-	Courant number
D	m	Fault displacement
$\widehat{e_z}$	m	Unit vector in z-direction
f_μ	-	Viscosity relation function
g	m/s^2	Gravitational acceleration
h	m	Hydraulic head *or* mesh element size
$\boldsymbol{K}$	m^2	Hydraulic conductivity tensor
L	m *or* -	Domain length *or* convection cell aspect ratio
$L_c^{(\min)}$	-	(minimum) Critical convection cell aspect ratio
Pe	-	Grid Péclet number
Q_{EB}	day^{-1}	Extended Boussinesq approximation term
$\overrightarrow{q^f}$	m/s	Specific discharge/Darcy velocity
q_H^f	W/m^2	Lower boundary constant heat flux
Ra	-	System Rayleigh number
$Ra_c^{(\min)}$	-	(minimum) Critical Rayleigh number
S_0	m^{-1}	Specific storage
$T_{(0)}$	°C	(reference) Temperature
T_d	-	Dilation tendency
T_s	-	Slip tendency
$\Delta t_{\max}$	day	Maximum time step for iteration
V_m and V_{clay}	- %	Effective and local clay content
$(\Delta)w$	m	(incremental change of) Fault width
$z_{(\max)}$	m	(maximum) burial depth
Greek symbols	**Unit**	**Description**
$\alpha_{L,T}$	m	Longitudinal and transversal thermal dispersivity
$\beta(T)$	K^{-1}	Thermal expansion coefficient (temperature dependent)
ε	-	Permeability contrast factor
$\lambda_{(m)}$	W/m/K	(effective) Thermal conductivity
λ^f and λ^s	W/m/K	Thermal conductivity of fluid and solid phase
Λ_{m}	m^2/s	Thermal diffusivity
μ_s	-	Friction coefficient
$\mu_{(0)}^f$	Pa·s	(reference) dynamic fluid viscosity
$\rho_{(0)}^f$ and ρ^s	kg/m^3	(reference) density for fluid and solid phase
$\sigma_{n(eff)}$ and $\sigma_{1,2,3}$	Pa	(effective) normal stress and principles stresses
τ	Pa *or* m	Shear stress *or* fault throw
φ	-	Porosity
Permeabilities	**Unit**	**Description**
$\boldsymbol{\kappa}$	m^2	Permeability tensor
κ_m	m^2	Effective basin permeability
κ^v and $\overline{\kappa^v}$	m^2	Vertical and average vertical permeability
κ^h and $\overline{\kappa^h}$	m^2	Horizontal and average horizontal permeability
κ_{hr}^h and κ_{hr}^v	m^2	Horizontal and vertical host rock permeability
κ_f^L and κ_f^T	m^2	Longitudinal and transversal fault zone permeability
ξ_{hr} and ξ_f	-	Host rock and fault permeability anisotropy

11. Appendices

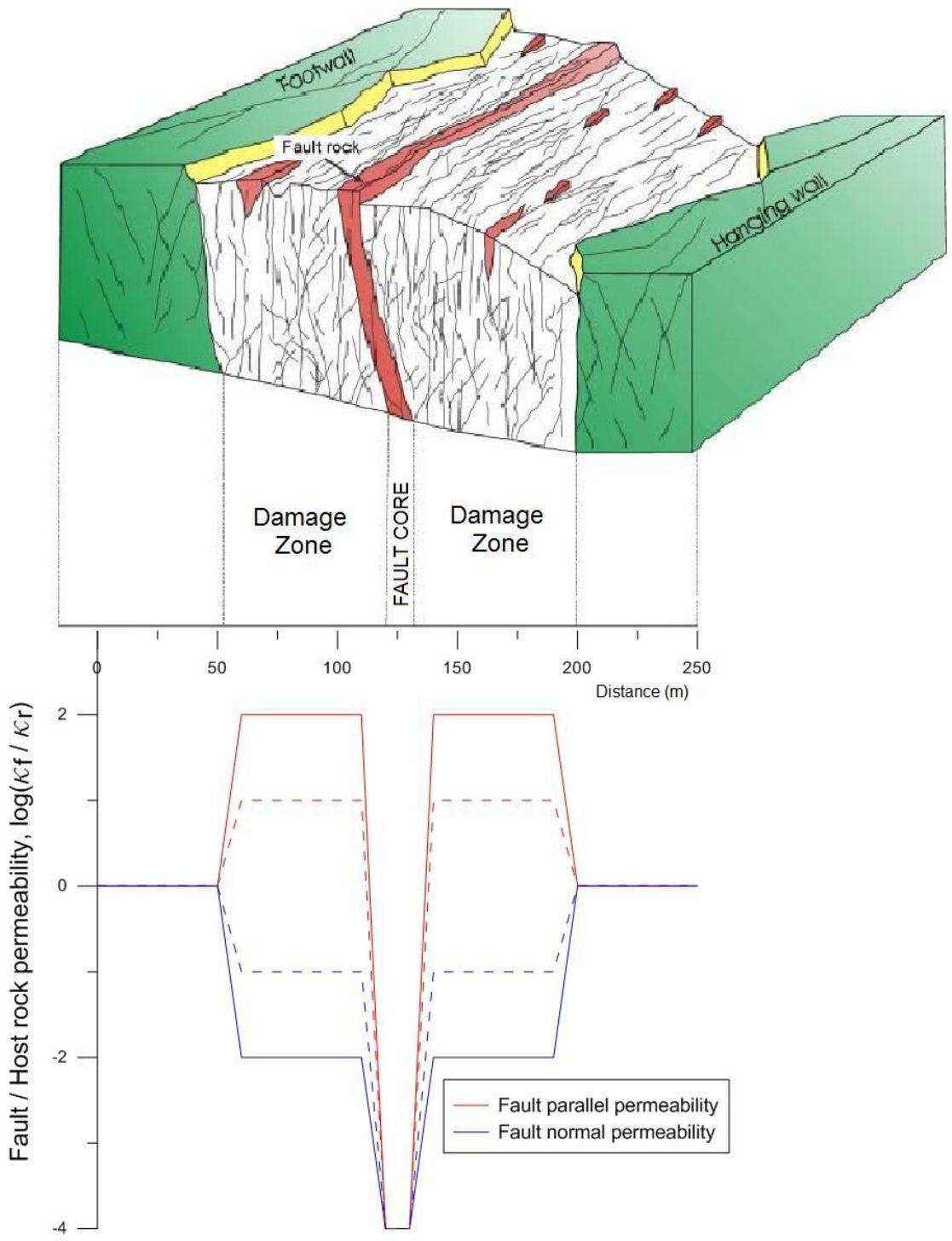

Appendix 1: Summarization of ranges for parallel and normal permeabilities normalized with host rock permeability for damage zone and fault core from Caine & Forster 1999; Atilla Aydin 2000; Flodin et al. 2001; Jourde et al. 2002

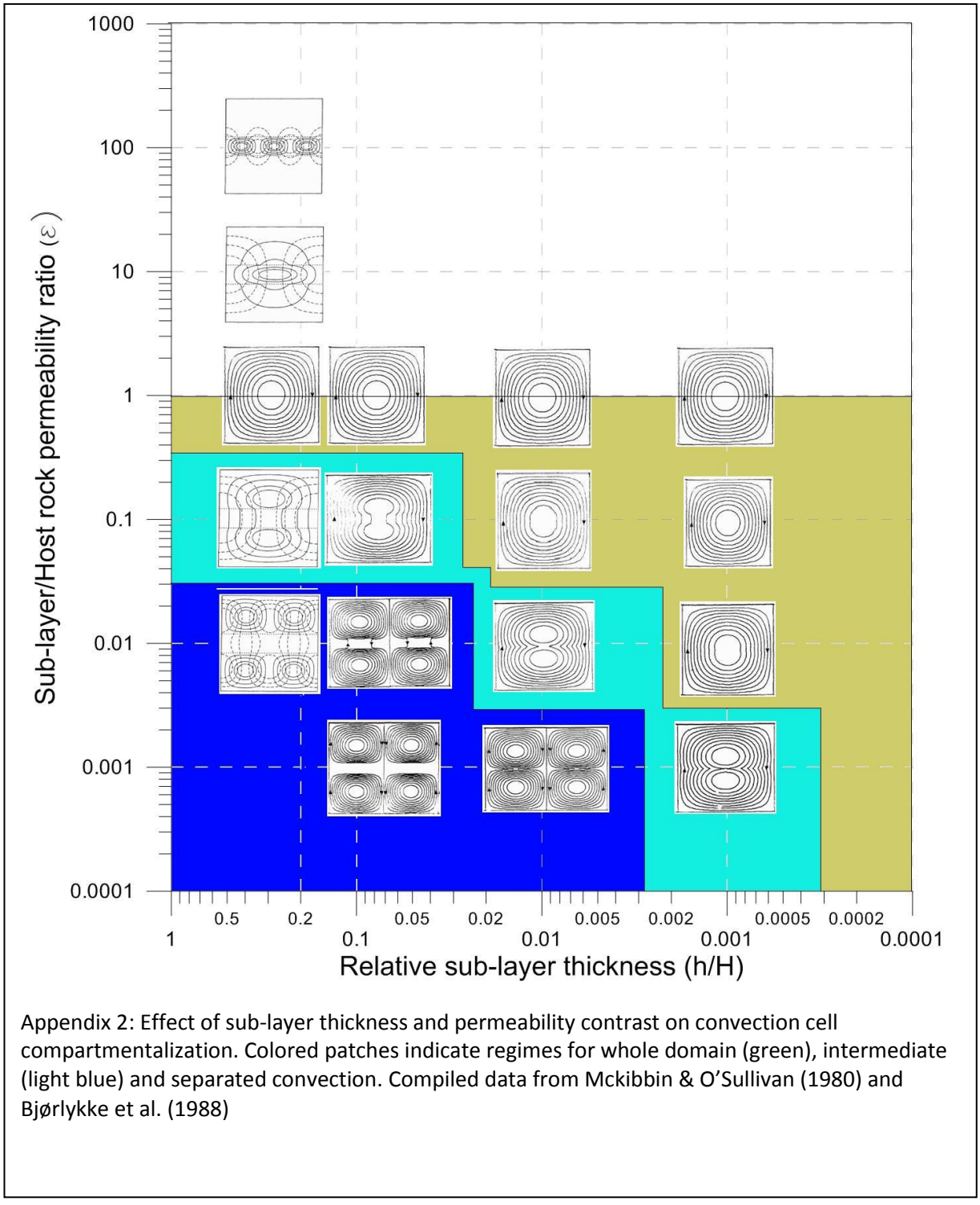

Appendix 2: Effect of sub-layer thickness and permeability contrast on convection cell compartmentalization. Colored patches indicate regimes for whole domain (green), intermediate (light blue) and separated convection. Compiled data from Mckibbin & O'Sullivan (1980) and Bjørlykke et al. (1988)

Appendix 3: Results

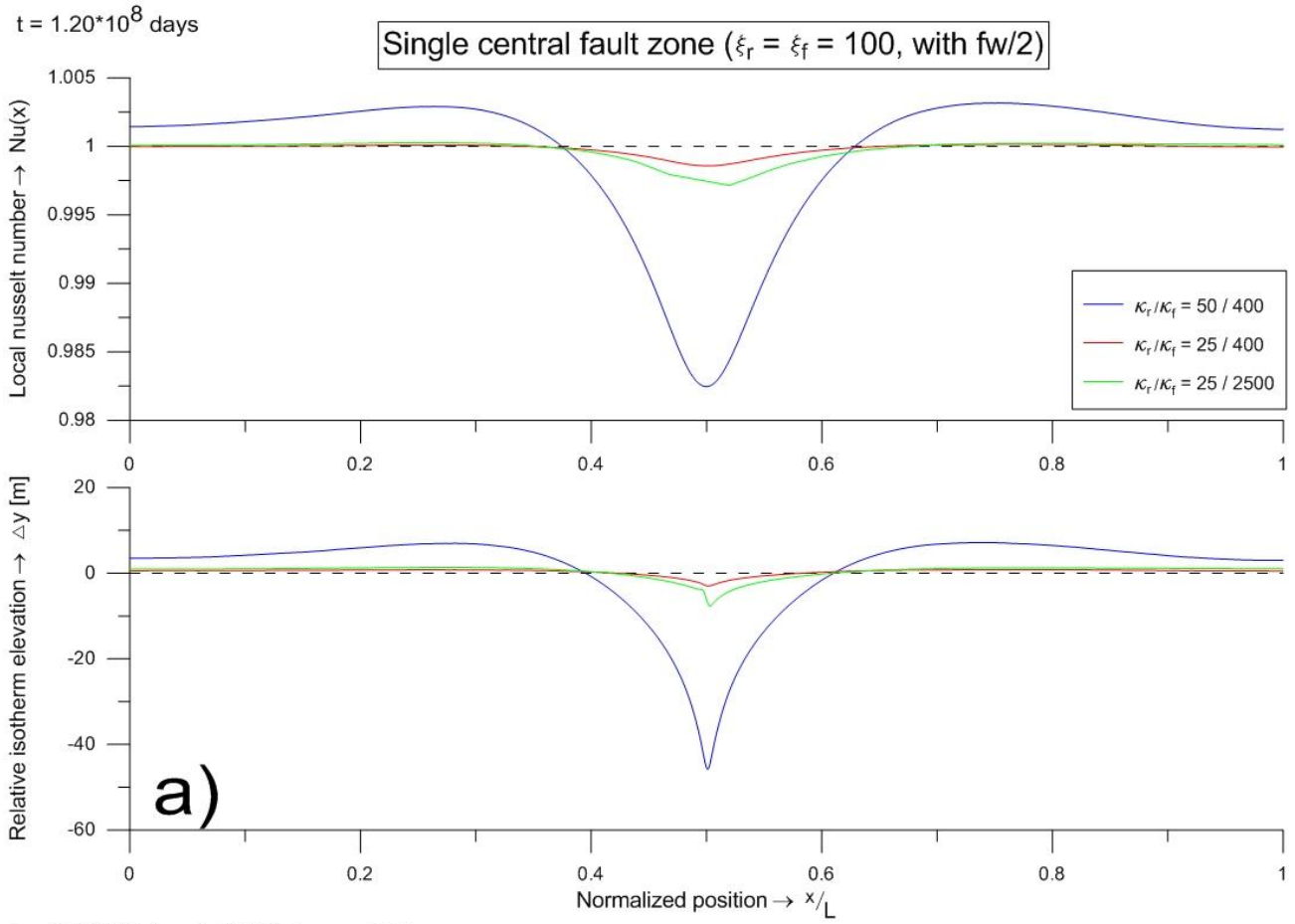

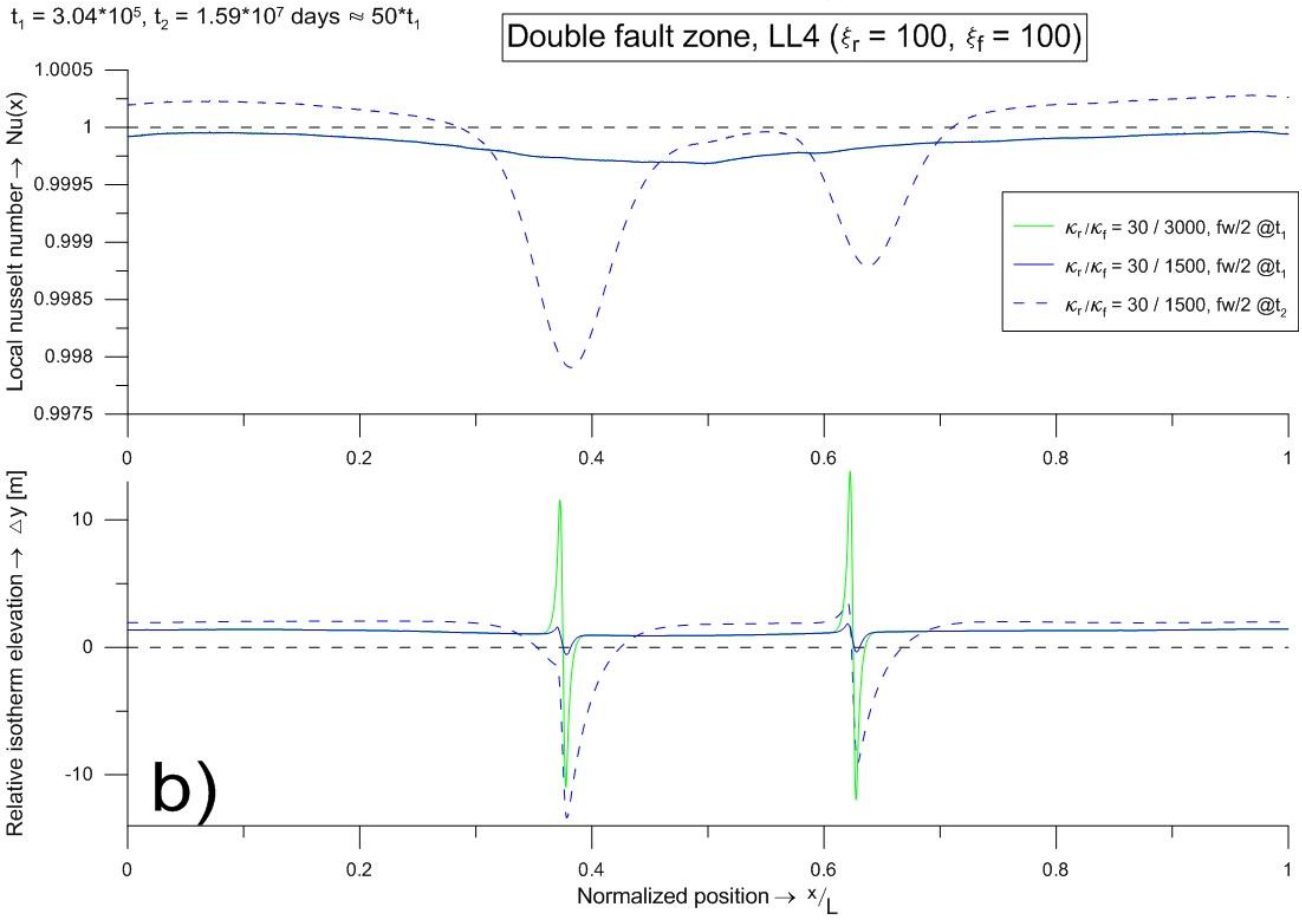

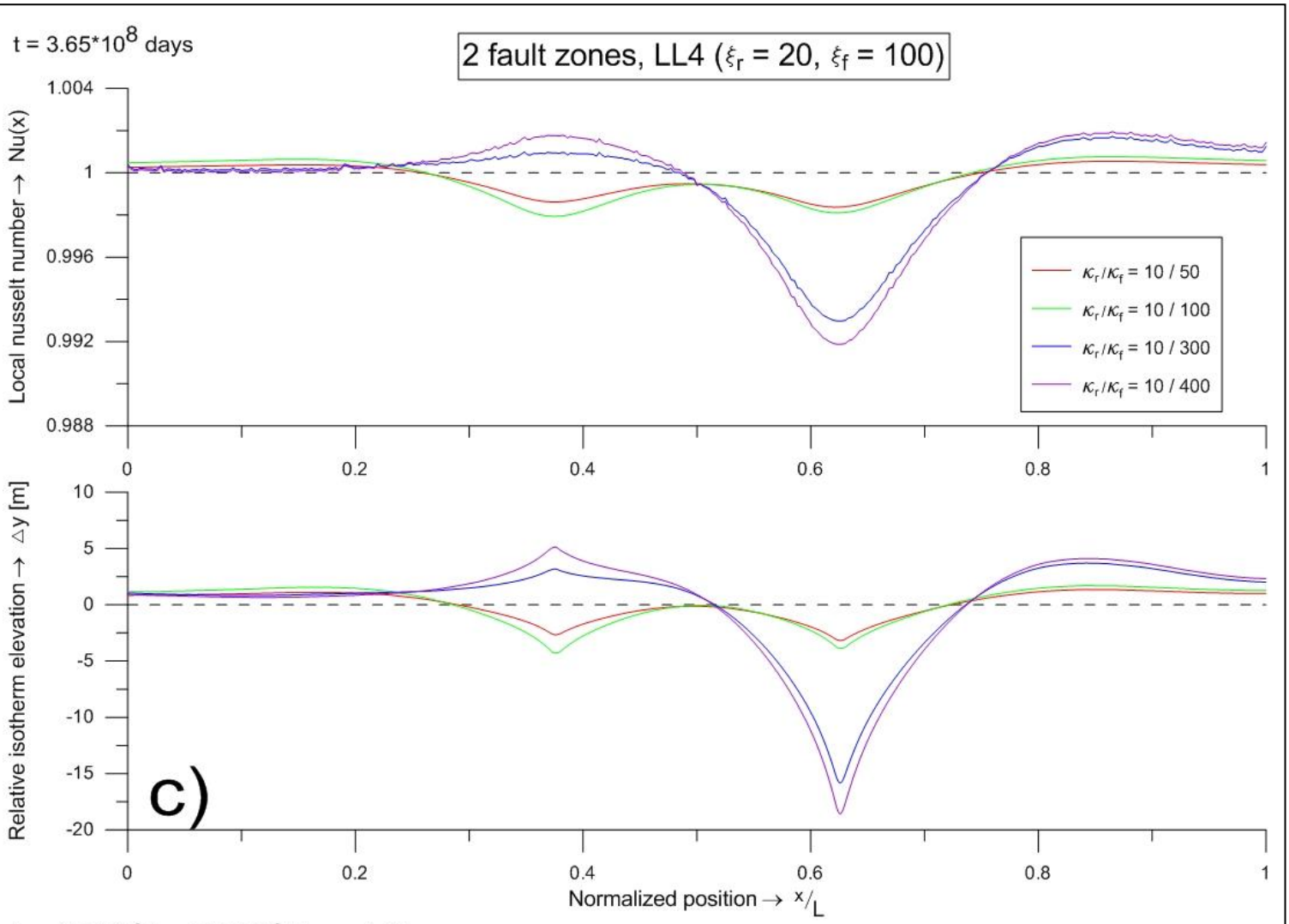
t = 3.65*10^8 days
2 fault zones, LL4 (ξr = 20, ξf = 100)
Local nusselt number → Nu(x)
1.004
1
0.996
0.992
0.988
κr/κf = 10 / 50
κr/κf = 10 / 100
κr/κf = 10 / 300
κr/κf = 10 / 400
0
0.2
0.4
0.6
0.8
1
Relative isotherm elevation → △y [m]
10
5
0
-5
-10
-15
-20
c)
Normalized position → x/L

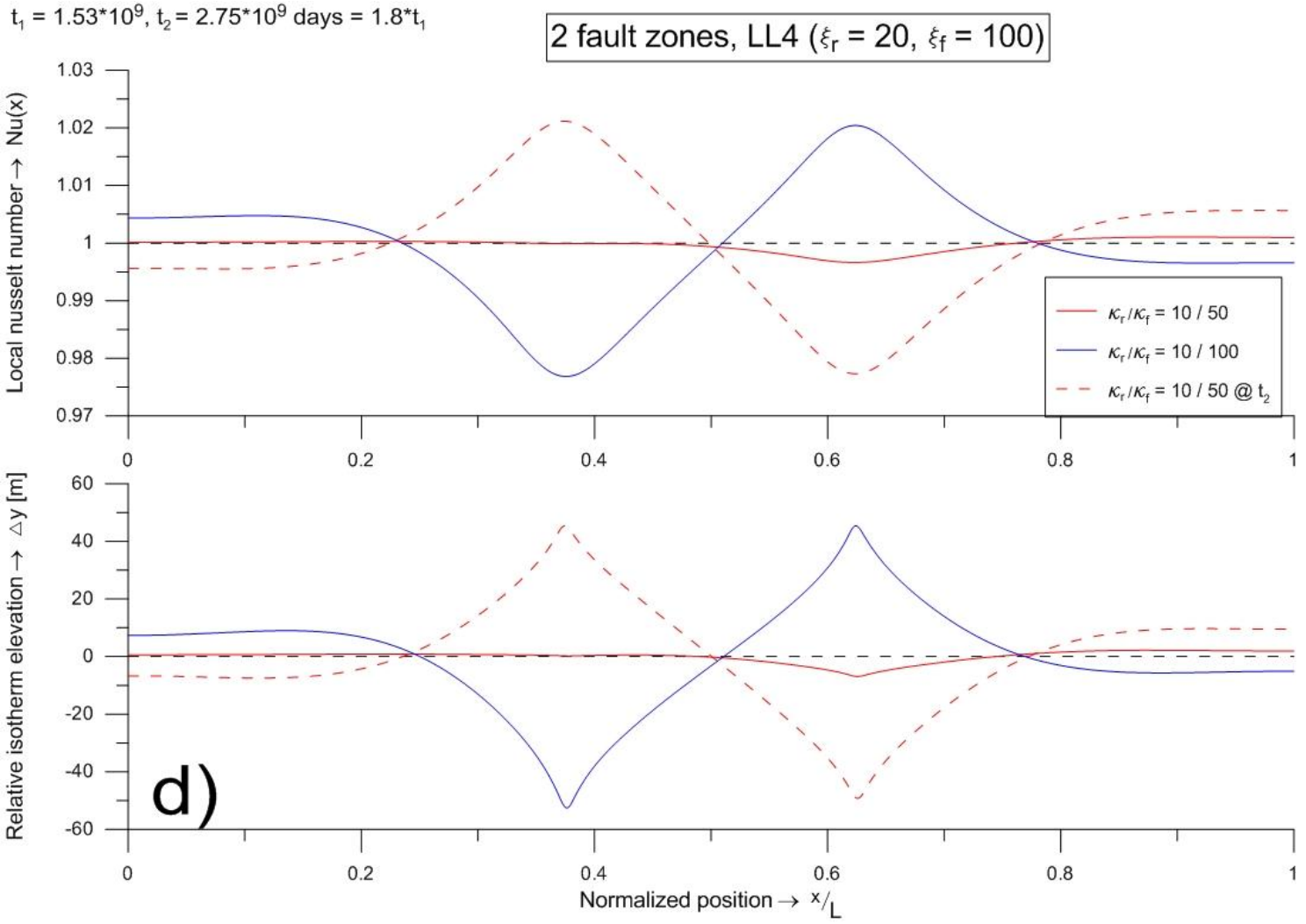
t1 = 1.53*10^9, t2 = 2.75*10^9 days = 1.8*t1
2 fault zones, LL4 (ξr = 20, ξf = 100)
Local nusselt number → Nu(x)
1.03
1.02
1.01
1
0.99
0.98
0.97
κr/κf = 10 / 50
κr/κf = 10 / 100
κr/κf = 10 / 50 @ t2
0
0.2
0.4
0.6
0.8
1
Relative isotherm elevation → △y [m]
60
40
20
0
-20
-40
-60
d)
Normalized position → x/L

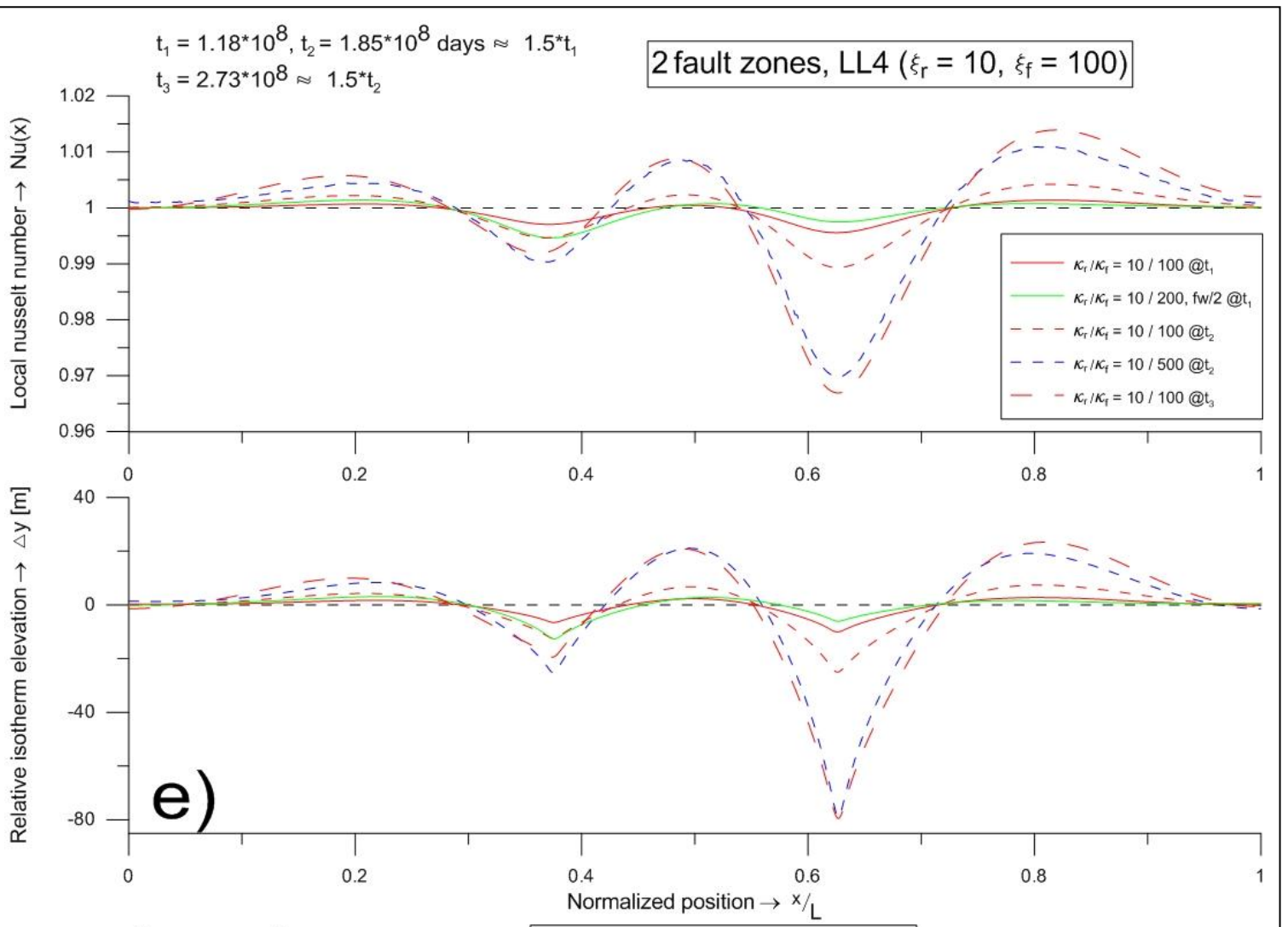
$t_1 = 1.18*10^8$, $t_2 = 1.85*10^8$ days ≈ $1.5*t_1$
$t_3 = 2.73*10^8$ ≈ $1.5*t_2$
2 fault zones, LL4 (ξ_r = 10, ξ_f = 100)
Local nusselt number → Nu(x)
κ_r/κ_f = 10 / 100 @t_1
κ_r/κ_f = 10 / 200, fw/2 @t_1
κ_r/κ_f = 10 / 100 @t_2
κ_r/κ_f = 10 / 500 @t_2
κ_r/κ_f = 10 / 100 @t_3
Relative isotherm elevation → △y [m]
e)
Normalized position → x/L

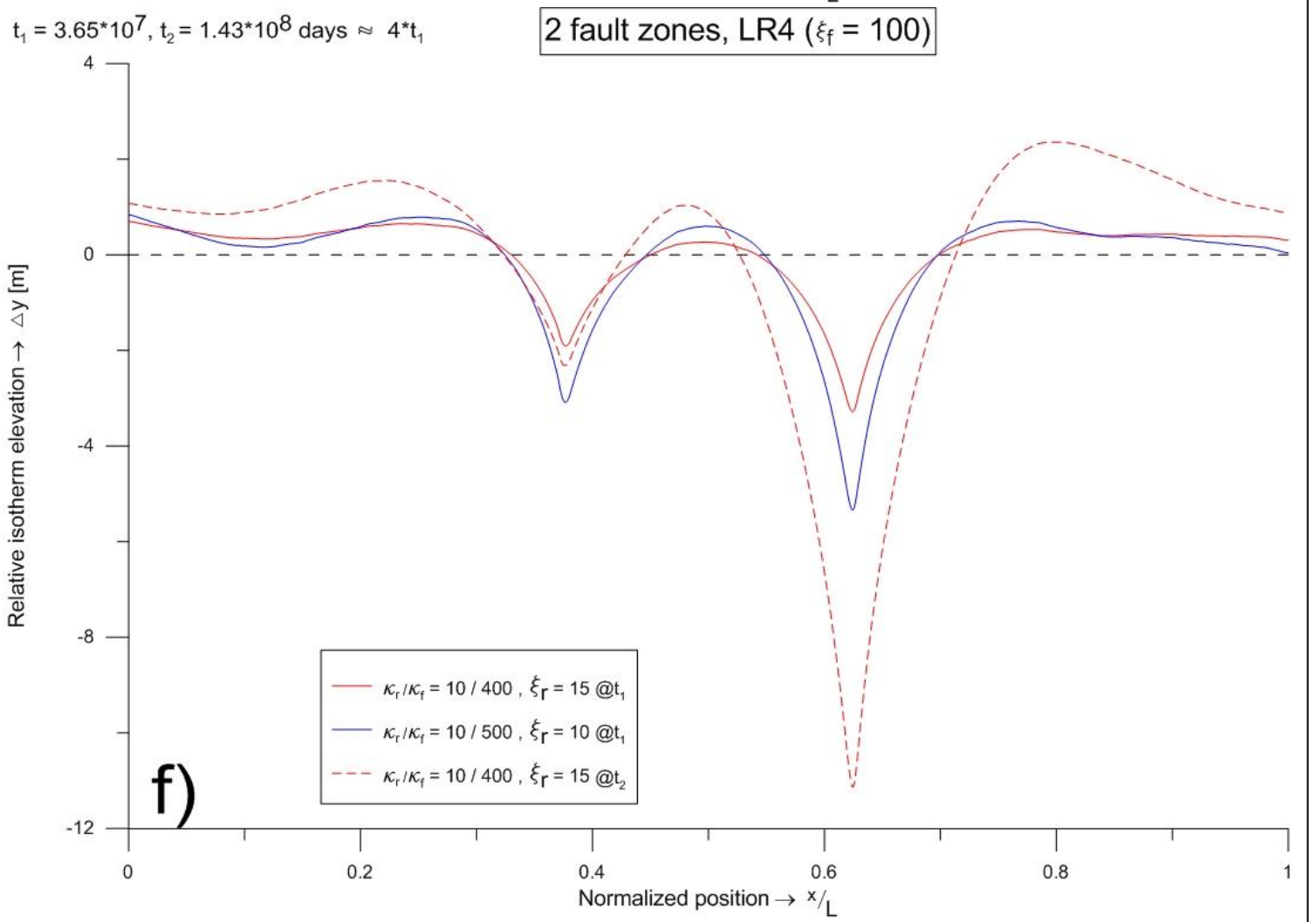
$t_1 = 3.65*10^7$, $t_2 = 1.43*10^8$ days ≈ $4*t_1$
2 fault zones, LR4 (ξ_f = 100)
Relative isotherm elevation → △y [m]
κ_r/κ_f = 10 / 400 , ξ_r = 15 @t_1
κ_r/κ_f = 10 / 500 , ξ_r = 10 @t_1
κ_r/κ_f = 10 / 400 , ξ_r = 15 @t_2
f)
Normalized position → x/L

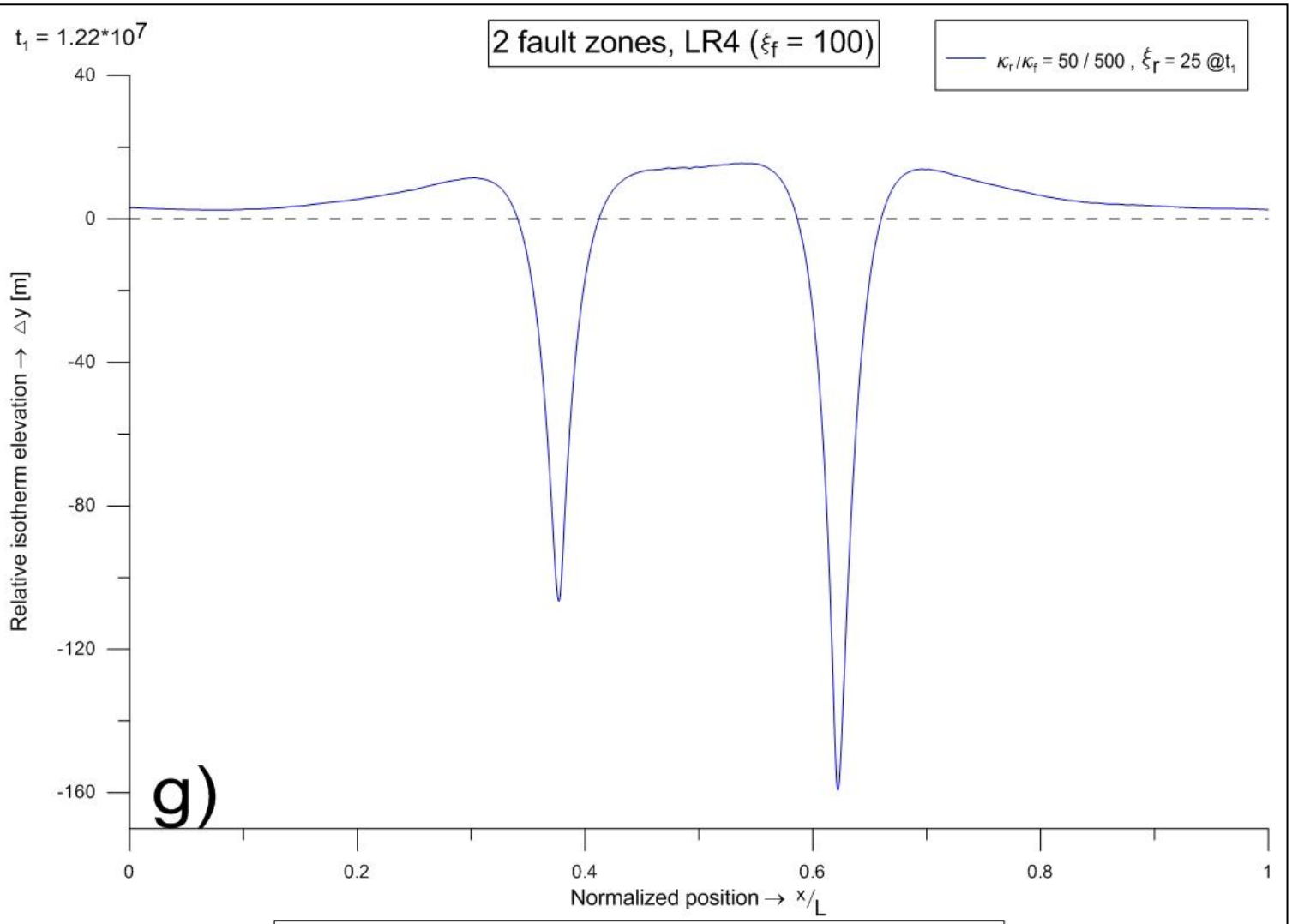
t1 = 1.22*10^7
2 fault zones, LR4 (ξf = 100)
κr/κf = 50 / 500 , ξr = 25 @t1
Relative isotherm elevation → △y [m]
40
0
-40
-80
-120
-160
g)
0
0.2
0.4
0.6
0.8
1
Normalized position → x/L

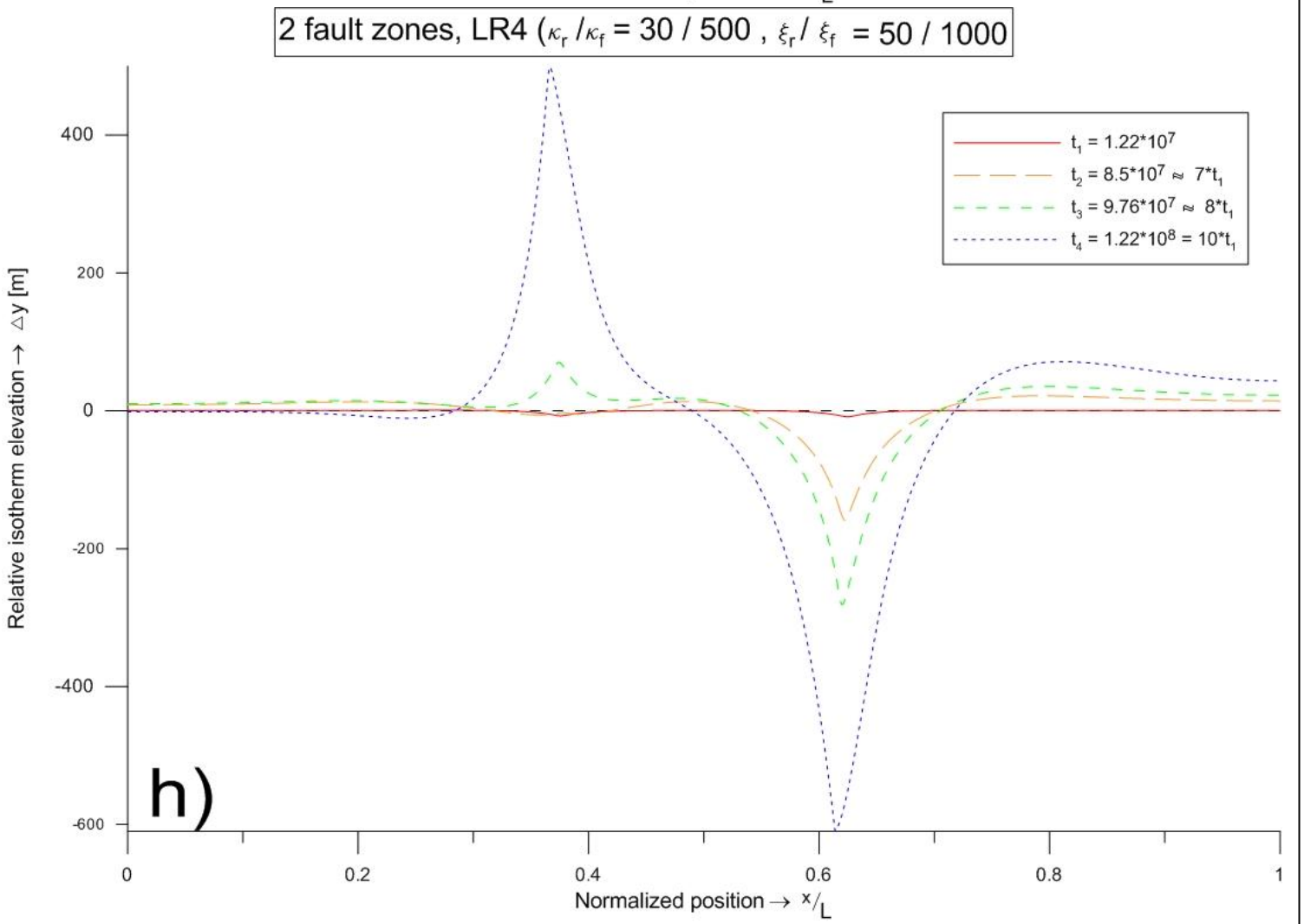
2 fault zones, LR4 (κr /κf = 30 / 500 , ξr / ξf = 50 / 1000
t1 = 1.22*10^7
t2 = 8.5*10^7 ≈ 7*t1
t3 = 9.76*10^7 ≈ 8*t1
t4 = 1.22*10^8 = 10*t1
Relative isotherm elevation → △y [m]
400
200
0
-200
-400
-600
h)
0
0.2
0.4
0.6
0.8
1
Normalized position → x/L

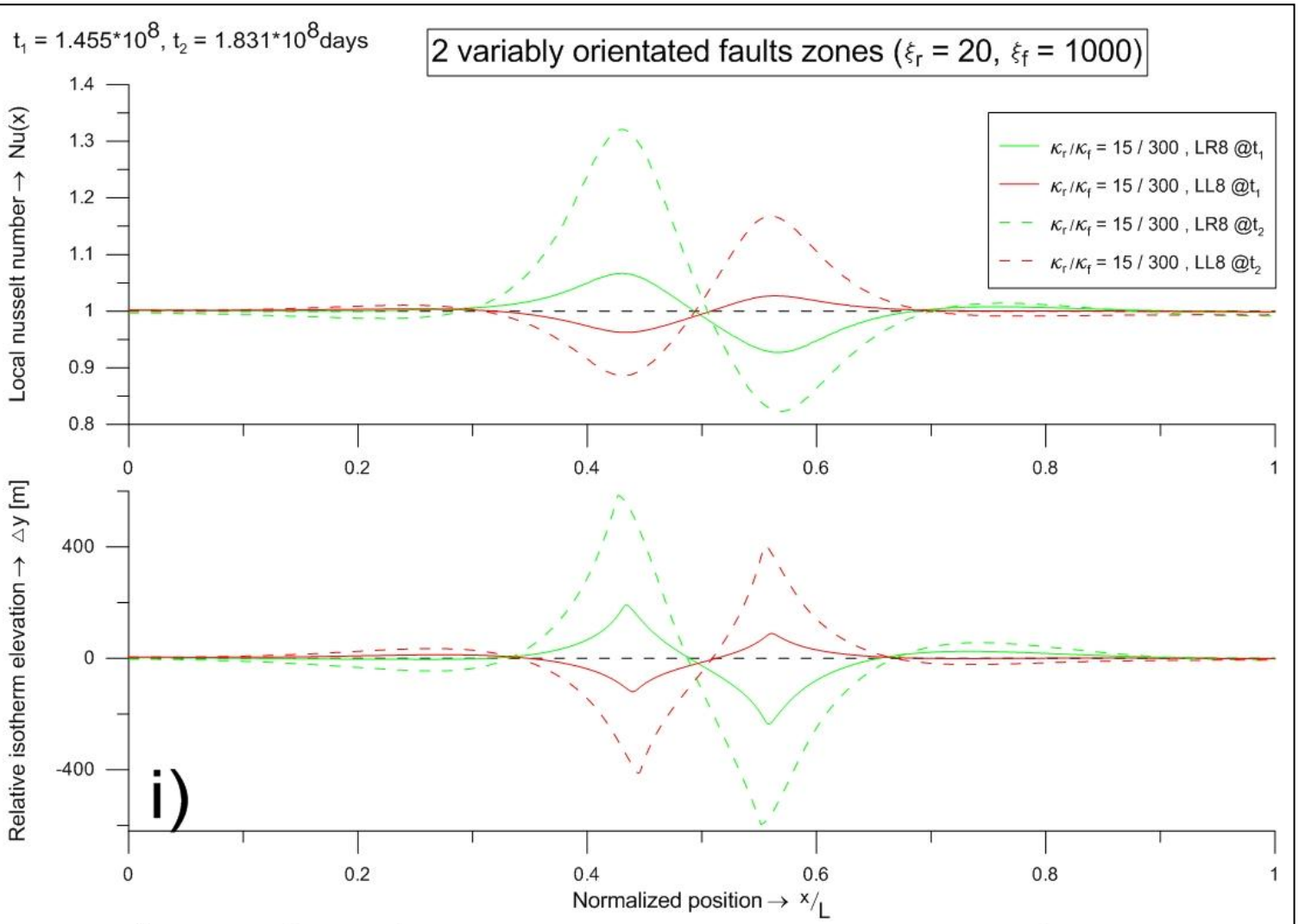
$t_1 = 1.455*10^8$, $t_2 = 1.831*10^8$days
2 variably orientated faults zones (ξ_r = 20, ξ_f = 1000)
Local nusselt number → Nu(x)
κ_r/κ_f = 15 / 300 , LR8 @t_1
κ_r/κ_f = 15 / 300 , LL8 @t_1
κ_r/κ_f = 15 / 300 , LR8 @t_2
κ_r/κ_f = 15 / 300 , LL8 @t_2
Relative isotherm elevation → △y [m]
i)
Normalized position → x/L

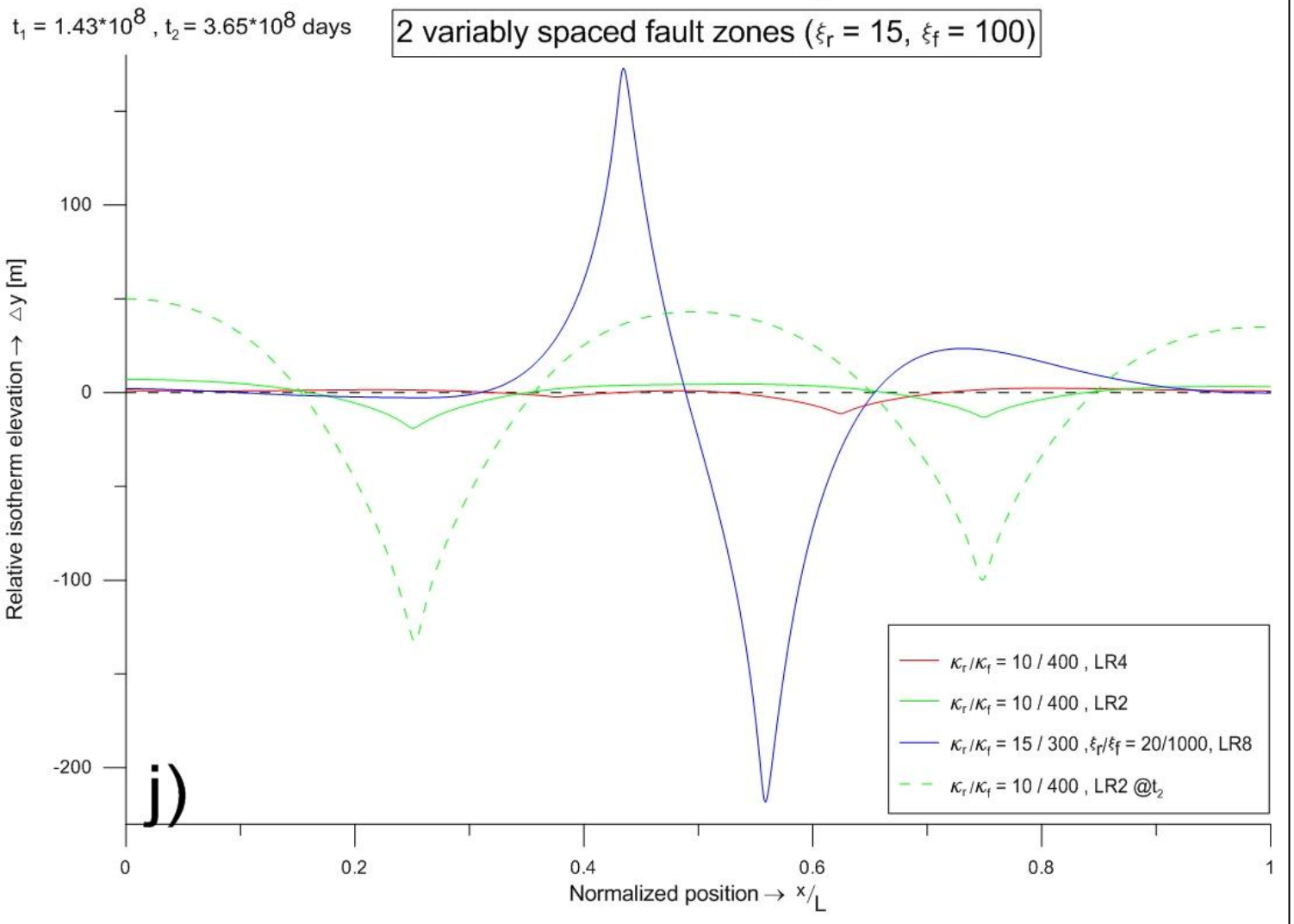
$t_1 = 1.43*10^8$, $t_2 = 3.65*10^8$ days
2 variably spaced fault zones (ξ_r = 15, ξ_f = 100)
Relative isotherm elevation → △y [m]
κ_r/κ_f = 10 / 400 , LR4
κ_r/κ_f = 10 / 400 , LR2
κ_r/κ_f = 15 / 300 , ξ_r/ξ_f = 20/1000, LR8
κ_r/κ_f = 10 / 400 , LR2 @t_2
j)
Normalized position → x/L

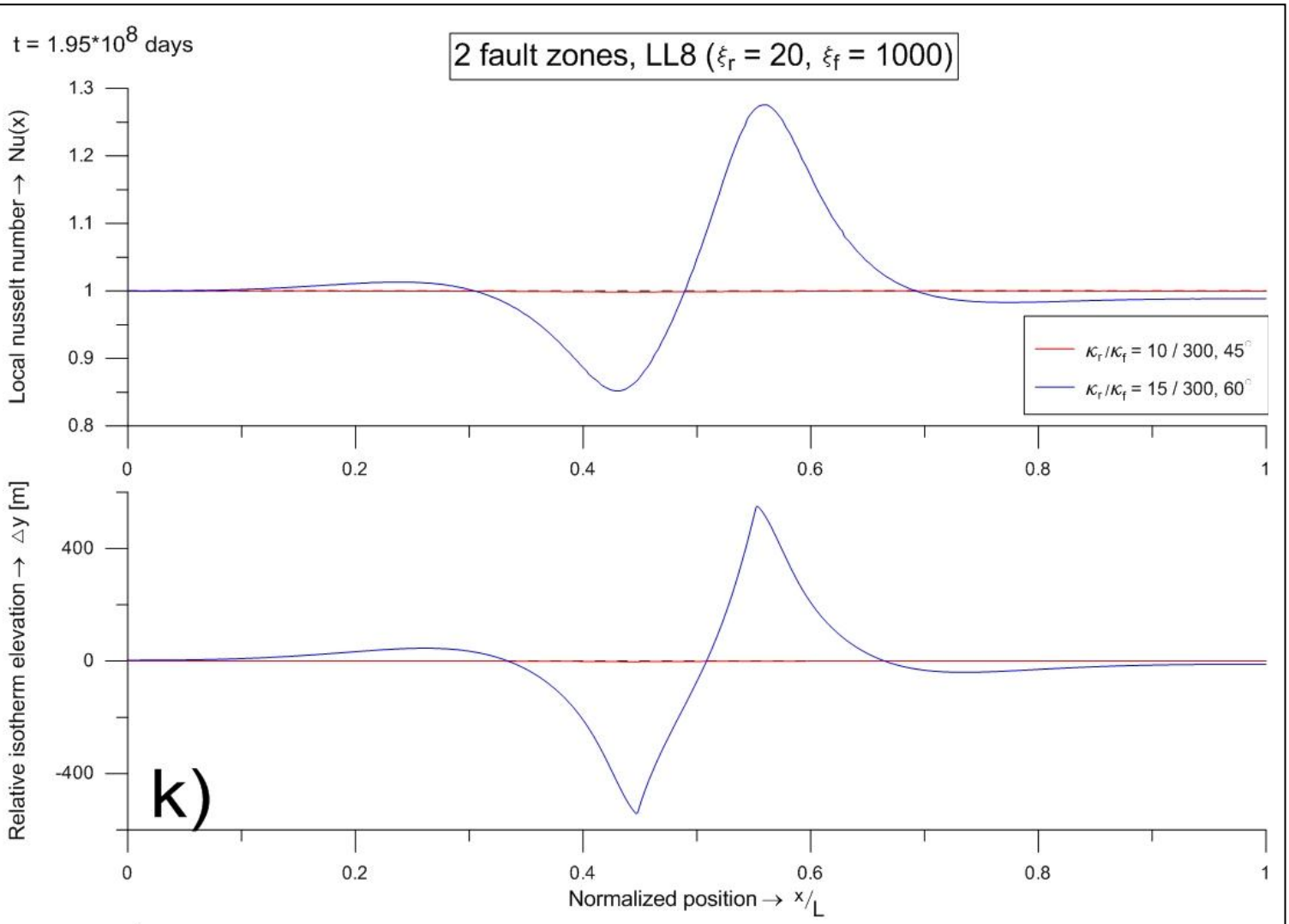
t = 1.95*10^8 days
2 fault zones, LL8 (ξr = 20, ξf = 1000)
Local nusselt number → Nu(x)
κr/κf = 10 / 300, 45°
κr/κf = 15 / 300, 60°
Relative isotherm elevation → △y [m]
k)
Normalized position → x/L

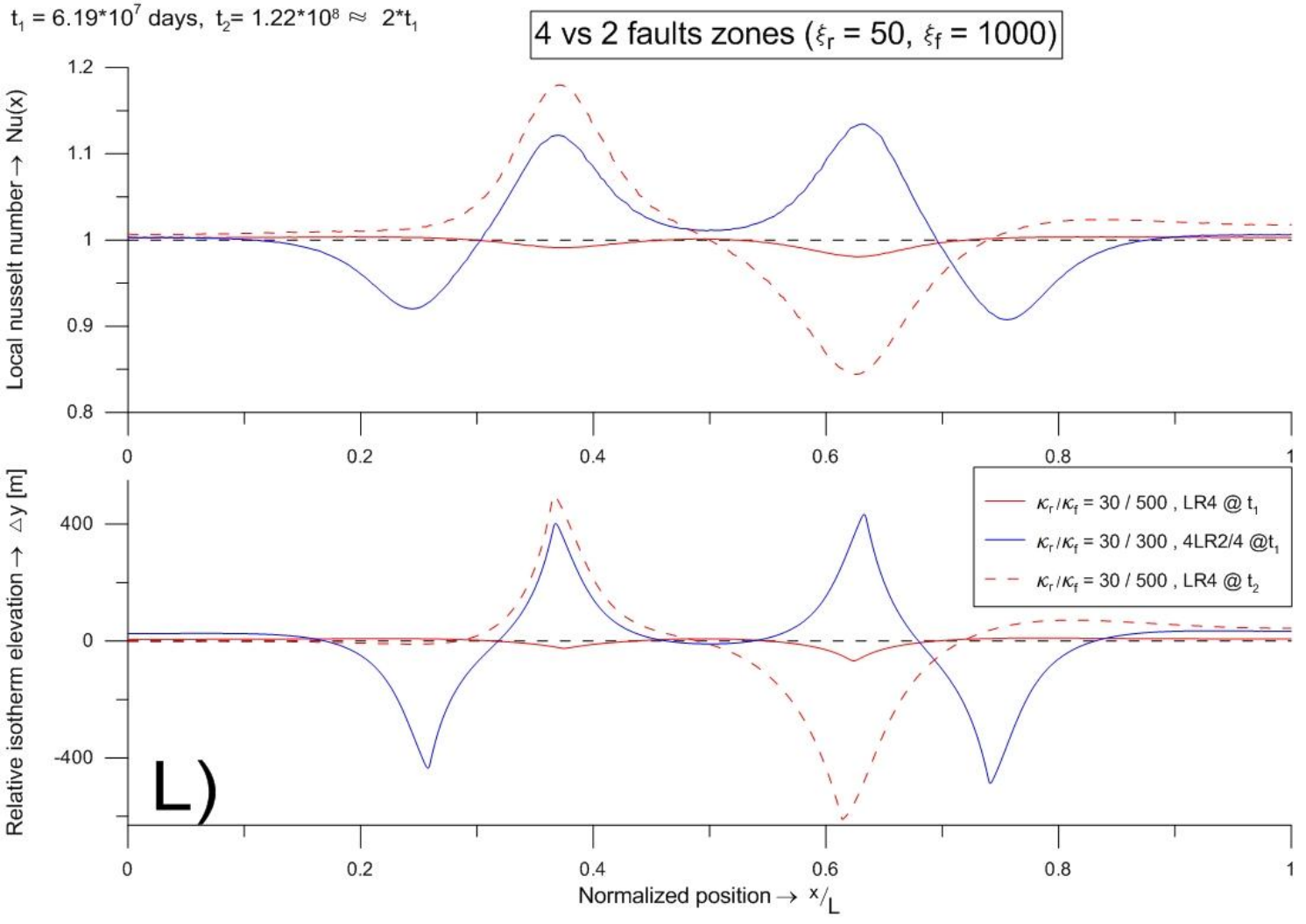
t1 = 6.19*10^7 days, t2= 1.22*10^8 ≈ 2*t1
4 vs 2 faults zones (ξr = 50, ξf = 1000)
Local nusselt number → Nu(x)
κr/κf = 30 / 500 , LR4 @ t1
κr/κf = 30 / 300 , 4LR2/4 @t1
κr/κf = 30 / 500 , LR4 @ t2
Relative isotherm elevation → △y [m]
L)
Normalized position → x/L

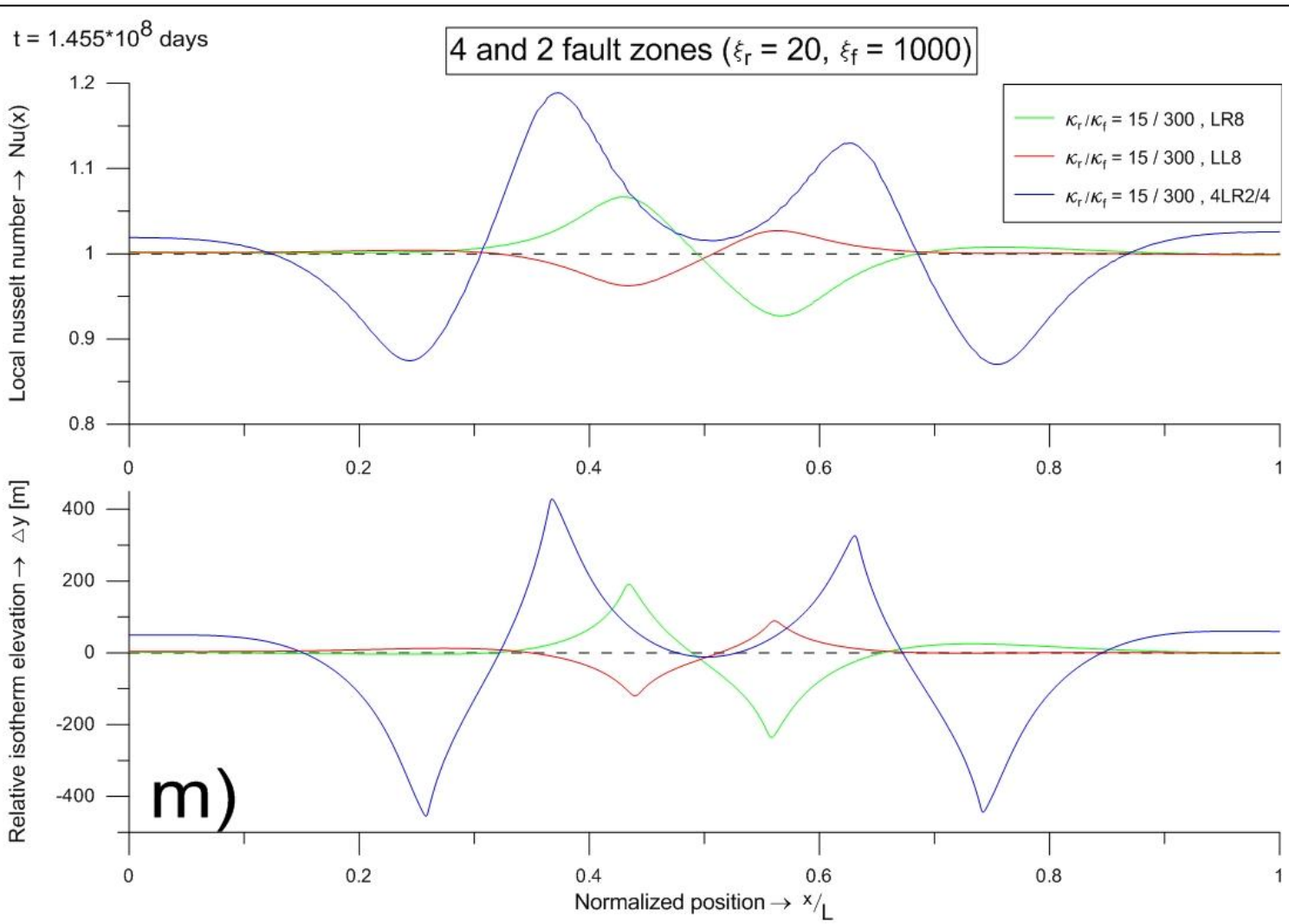
t = 1.455*10^8 days
4 and 2 fault zones (ξr = 20, ξf = 1000)
κr/κf = 15 / 300 , LR8
κr/κf = 15 / 300 , LL8
κr/κf = 15 / 300 , 4LR2/4
Local nusselt number → Nu(x)
Relative isotherm elevation → △y [m]
m)
Normalized position → x/L

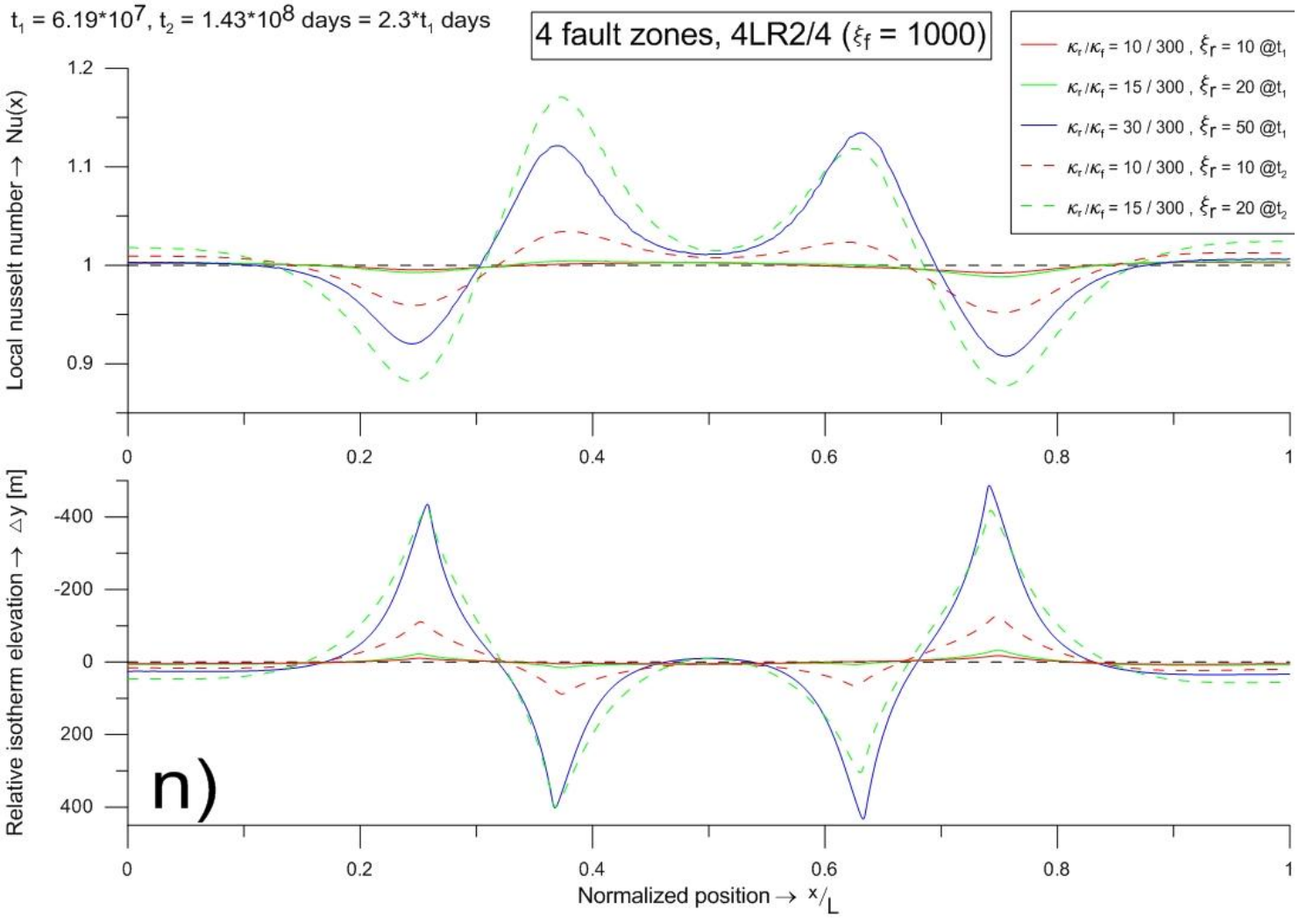
t1 = 6.19*10^7, t2 = 1.43*10^8 days = 2.3*t1 days
4 fault zones, 4LR2/4 (ξf = 1000)
κr/κf = 10 / 300 , ξr = 10 @t1
κr/κf = 15 / 300 , ξr = 20 @t1
κr/κf = 30 / 300 , ξr = 50 @t1
κr/κf = 10 / 300 , ξr = 10 @t2
κr/κf = 15 / 300 , ξr = 20 @t2
Local nusselt number → Nu(x)
Relative isotherm elevation → △y [m]
n)
Normalized position → x/L